UNIVERSIDADE ESTADUAL DE CAMPINAS
Instituto de Física “Gleb Wataghin”

GABRIEL PEREIRA FREITAS

GAS INTERACTIONS WITH THE SURFACE OF BLACK PHOSPHORUS

INTERAÇÃO DE GASES COM A SUPERFÍCIE DO FÓSFORO NEGRO

CAMPINAS
2018

GABRIEL PEREIRA FREITAS

GAS INTERACTIONS WITH THE SURFACE OF BLACK PHOSPHORUS

INTERAÇÃO DE GASES COM A SUPERFÍCIE DO FÓSFORO NEGRO

Dissertation presented to the "Gleb Wataghin" Institute of Physics of the University of Campinas in partial fulfillment of the requirements for the degree of Master in Physics, in the area of Applied Physics.

Dissertação apresentada ao Instituto de Física "Gleb Wataghin"da Universidade Estadual de Campinas como parte dos requisitos exigidos para a obtenção do título de Mestre em Física, na Área de Física Aplicada.

Supervisor/Orientador: PROF. DR. TÚLIO COSTA RIZUTI DA ROCHA
Co-supervisor/Coorientador: PROF. DR. ABNER DE SIERVO

ESTE EXEMPLAR CORRESPONDE À VERSÃO FINAL DA DISSERTAÇÃO DEFENDIDA PELO ALUNO GABRIEL PEREIRA FREITAS, ORIENTADA PELO DR. TÚLIO COSTA RIZUTI DA ROCHA, E COORIENTADA PELO DR. ABNER DE SIERVO

CAMPINAS
2018

Agência(s) de fomento e nº(s) de processo(s): FAPESP, 2016/06798-2; CAPES, 1583453/2016

Ficha catalográfica
Universidade Estadual de Campinas
Biblioteca do Instituto de Física Gleb Wataghin
Lucimeire de Oliveira Silva da Rocha - CRB 8/9174

F884g

Freitas, Gabriel Pereira, 1993-
Gas interactions with the surface of black phosphorus / Gabriel Pereira Freitas. – Campinas, SP : [s.n.], 2018.

Orientador: Tulio Costa Rizuti da Rocha.
Coorientador: Abner de Siervo.
Dissertação (mestrado) – Universidade Estadual de Campinas, Instituto de Física Gleb Wataghin.

1. Espectroscopia de elétrons fotoemitidos por raios-X. 2. Semicondutores. 3. Fotoxidação. I. Rocha, Tulio Costa Rizuti da, 1979-. II. Siervo, Abner de, 1972-. III. Universidade Estadual de Campinas. Instituto de Física Gleb Wataghin. IV. Título.

Informações para Biblioteca Digital

Título em outro idioma: Interação de gases com a superfície do fósforo negro
Palavras-chave em inglês:
X-ray photoelectron spectroscopy
Semiconductors
Photooxidation
Área de concentração: Física Aplicada
Titulação: Mestre em Física
Banca examinadora:
Tulio Costa Rizuti da Rocha [Orientador]
Jonder Morais
Cris Adriano
Data de defesa: 13-09-2018
Programa de Pós-Graduação: Física

MEMBROS DA COMISSÃO JULGADORA DA DISSERTAÇÃO DE MESTRADO DE **GABRIEL PEREIRA FREITAS – RA 164179** APRESENTADA E APROVADA AO INSTITUTO DE FÍSICA "GLEB WATAGHIN", DA UNIVERSIDADE ESTADUAL DE CAMPINAS, EM 13 / 09 / 2018.

COMISSÃO JULGADORA:

- Prof. Dr. Tulio Costa Rizuti da Rocha – Orientador – CNPEM/LNLS
- Prof. Dr. Jonder Morais – IF/UFRGS
- Profa. Dra. Cris Adriano – IFGW/UNICAMP

OBS.: Informo que as assinaturas dos respectivos professores membros da banca constam na ata de defesa já juntada no processo vida acadêmica do aluno.

CAMPINAS
2018

Acknowledgements

I would like to thank the following people:

My parents and sisters, without you I would never have reached this far, or anywhere at all.

My grandmother, who were always there when I needed someone to talk to. And also my grandfather, who I knew was looking down upon me this whole time.

Renata, for standing by my side throughout these master's years, whose support made things much more bearable.

My colleagues from the good old days of the physics undergrad studies at UFPR. Specially Matheus, Jean and Kevin who continued with me at Unicamp.

My colleagues from the grad school at Unicamp, for the companionship and for the fun days studying quantum mechanics together. Who are so many I will not venture myself into listing you.

The secretary of the grad school of physics from IFGW. Whenever I needed, they were there for me.

The professors at Unicamp who one way or another contributed to my academic formation. Including my co-supervisor Abner de Siervo.

The administration and direction of the LNLS laboratory at CNPEM.

All the members, past and present, of the SIMM group at LNLS. All of you contributed to this master project and/or to my knowledge. I'll always regard fondly of you.

Wendell and Fernando for helping out with the experiments at SOLEIL. And Travis for providing us with very useful DFT calculations.

The author would like to acknowledge the São Paulo Research Foundation (FAPESP) for the funding of this master project through the process 2016/06798-2. This study was financed in part by the Coordenação de Aperfeiçoamento de Pessoal de Nível Superior - Brasil (CAPES) - Finance Code 001.

At last, I would like to thank my advisor Tulio. You taught me everything I needed and more. You were there for me every inch of the way. And gave me courage to pursue things when they seemed too ambitious. To have your name in my academic records is a life lasting honor.

Resumo

Fósforo Negro (BP) é um semicondutor de multi-camadas, onde cada mono-camada é denominada fosforeno. Ao contrário do grafeno, BP apresenta um *bandgap* direto na região da luz-visível modificável de acordo com o número de camadas. As duas direções distintas no plano da superfície de *van-der-Waals* produzem uma anisotropia intrínseca da mobilidade de portadores. Como um material bidimensional complementar, BP é relevante para aplicações em eletrônica de alta-frequência. No entanto, BP é instável em condições ambientes, oxidando e sofrendo completa degradação. Oxigênio, água e luz são fatores importantes no processo de oxidação, embora o mecanismo de reação ainda não é completamente entendido. Por outro lado, a presença de uma camada de óxido isolante crescido de forma controlada pode ser uma vantagem. Neste trabalho realizamos experimentos de espectroscopia de fotoemissão em pressão ambiente (AP-XPS) com luz síncrotron para estudar a oxidação do BP sob uma atmosfera controlada. Usando informações sobre estequiometria e energias de ligação, em conjunto com cálculos de DFT, nós investigamos a estrutura atômica e eletrônica do óxido de fosforeno (PO) e da heteroestrutura com o BP. Quando exposto à uma atmosfera de água deoxigenada, não observamos nenhuma oxidação. Por outro lado, quando exposto à uma atmosfera de oxigênio seco, uma camada de PO cresceu até uma espessura de 1.35 nm depois de 2.5 horas. Adiante, nenhuma oxidação ocorreu após a formação de uma camada de passivação. Utilizando dados de estequimoetria determinados pelo AP-XPS, nós propusemos uma estrutura atômica sem precedente, o P_4O_8. Essa estrutura é corroborada por cálculos de DFT. Notavelmente, medidas espectroscópicas em função da profundidade abaixo da superfície mostraram deslocamentos de níveis de caroço e de banda de valência, tanto para o óxido quanto para o fósforo negro, da ordem de 0.2 eV. Esses deslocamentos diminuem para camadas mais profundas. Em sumário, nossos resultados indicaram o crescimento de uma camada passivadora de PO, que modifica a estrutura eletrônica das camadas de fosforeno abaixo. Essas descobertas podem ajudar futuras pesquisas de dispositivos baseados em BP ao controlar o crescimento do óxido e arranha a superfície das investigações da química de superfície desse material.

Abstract

Black Phosphorus (BP) is a semiconductor with a stacked layers structure, wherein each monolayer is denominated Phosphorene. Unlike graphene, BP presents a thickness-tunable direct band gap in the visible range. The two distinct in-plane directions of the van-der-Waals surface yields intrinsic anisotropic carrier mobility. As a complementary 2D material, BP is relevant for applications in high-frequency electronics. However, BP is unstable at ambient conditions, oxidizing and suffering complete degradation. Oxygen, water and light play important roles on the oxidation process, although the mechanism itself is yet to be fully understood. In this work we used synchrotron based ambient-pressure X-ray photoemission spectroscopy (AP-XPS) to study the BP oxidation under a controlled environment. Using the stoichiometry and binding energies, assisted by DFT calculations, we investigate the atomic and electronic structures of the phosphorene oxide (PO) and BP heterostructure. When solely exposing BP to oxygen-free water, we observed no oxidation. On the other hand, when exposing to dry oxygen, a layer of PO grew to a thickness of 1.35 nm after 2.5 hours. Furthermore, no oxidation takes place after this passivation layer has been established. Using stoichiometry ratios determined from AP-XPS, we propose an unprecedented atomic structure for this oxide, the P_4O_8 that agrees well with DFT calculations. Remarkably, depth dependent AP-XPS measurements showed shifts in the core and valence level binding energies of the order of 0.2 eV at the interface that decreases for deeper layers. These shifts suggest that a charge transfer occurs at the interface. In summary, our results indicate the growth of a passivating insulator layer of PO, that modifies the electronic structure of the underlying phosphorene layers. These discoveries can assist further research of BP-based devices by controlling the oxide growth and give insights for future investigations of the surface chemistry.

List of Figures

List of Tables

Contents

Chapter 1

Introduction

1.1 Black Phosphorus

Black Phosphorus (BP) is the most thermodynamically stable allotrope of phosphorus; it is kinetically inert and does not self-ignite in air at temperatures as high as 670 K [1]. It appears mainly as a metallic dark crystal with a flat surface or a polycrystalline needle structure, depending upon its synthesis method [2]. Black Phosphorus has a stacked layers structure that resembles that of graphite, with a single structural unit, or monolayer, stacked on top of each other bounded by *van-der-Waals* force (Figure 1.1). Likewise, each monolayer of BP is denominated phosphorene, in homage to graphene.

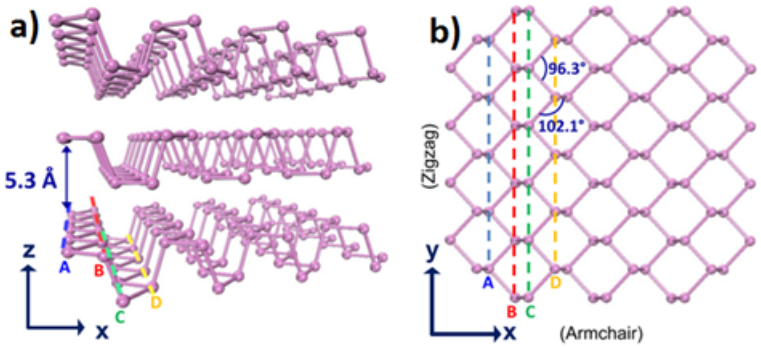

Figure 1.1: a) Side view of Black Phosphorus. b) Top view of a monolayer (phosphorene) with its two distinct planar directions. Adapted from reference [3].

Each phosphorus atom in this allotrope presents sp^3 hybridization with two in-plane interatomic bonds, one off-plane interatomic bond and one electron lone-pair, as shown in Figure 1.2. This configuration renders phosphorene with two distinct in-plane directions, the armchair and the zig-zag (Figure 1.1-b)[4]. Black phosphorus has been known for more than 100 years since it was first synthesized by Bridgman in 1914 [2]. Since then, little attention has been given to this material, and research was limited to high pressure physics. With the sprout of the 2D materials revolution led by the discoveries of exciting properties of graphene, black phosphorus and phosphorene have been revisited [3]. Similarly to graphite, black phosphorus

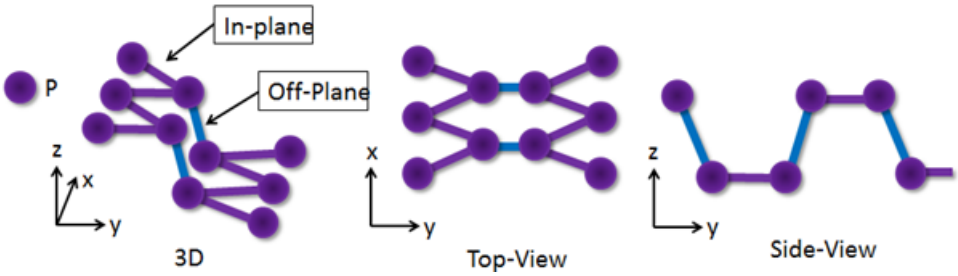

Figure 1.2: Atomic bonds of phosphorene. Bond angles and lengths not to scale.

is prone to cleaving, an easy way of obtaining its 2D counterparts. Nevertheless, more efficient methods of growth or isolation of phosphorene are still a hot topic of research.

Unlike graphene that is a good conductor, black phosphorus is a semiconductor. One of black phosphorus's most promising properties is the thickness-tunable direct bandgap in the near-infrared and visible range. Whereas bulk black phosphorus presents a bandgap of 0.3 eV, a monolayer phosphorene presents a bandgap of approximately 2 eV. As we add layers of phosphorene, the van-der-Waals interactions promote a band splitting over the Brillouin zones, decreasing the bandgap at the Γ points (Figure 1.3) [5, 6].

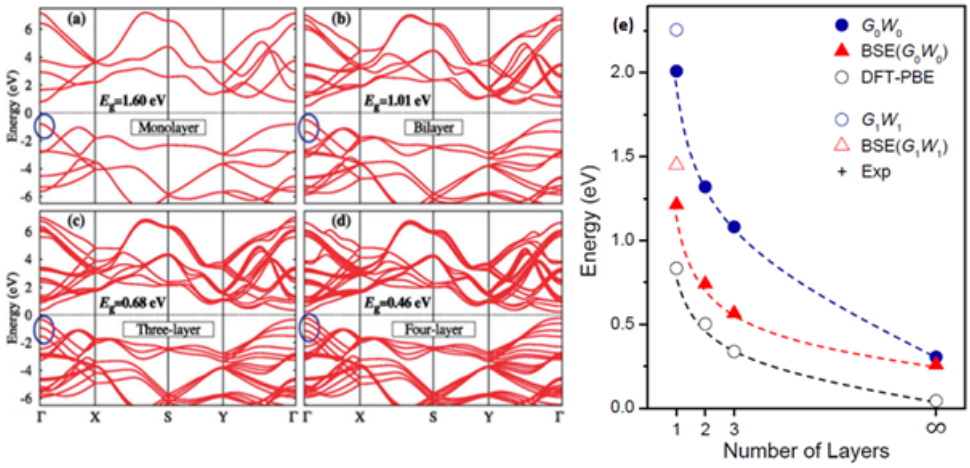

Figure 1.3: Calculated bandgap of phosphorene with 1 (a), 2 (b), 3 (c) and 4 (d) layers. As layers are added, the bandgap closes towards its bulk limit of approximately 0.3 eV. As also evidenced by different calculations shown in (e). Adapted from reference [5].

This tunable gap of black phosphorus is complementary to other members of the family of 2D materials. Black phosphorus's 0.3-2 eV bandgap fills a technological void that was left by the non-existent gap in the graphene, the 1.0-2.5 eV gap of the transition metal dichalcogenides (TMDC) and the 6 eV gap of hexagonal boron-nitride (hBN) [7], as we can see in Figure 1.4. Strain has been shown to be an effective way of further tuning the bandgap of black phosphorus, changing both the band gap size [8] and it's direct-indirect transition [9]. Both compressive and tensile strains applied mainly to few layers broadens the bandgap range, increasing its capability of applications [3].

Furthermore, the carrier mobility was evaluated both by experimental [10–14] and

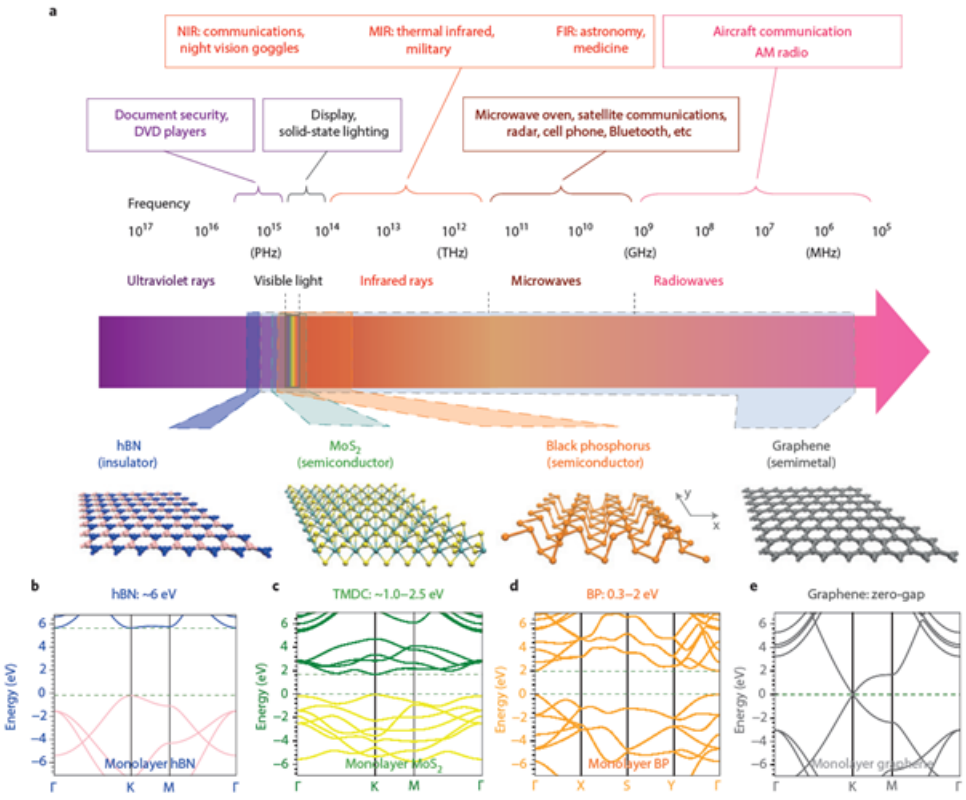

Figure 1.4: a) Electromagnetic spectrum with applications assigned to different spectrum ranges, with the ranges of some 2D materials, such as hBN, MoS2, Black phosphorus and Graphene shown. Band structure of hBN (b), MoS2 (c), BP (d) and graphene (e). Adapted from reference [7].

theoretical [15] works. The different in-plane directions of phosphorene render anisotropic behaviour to its charge mobility, with each direction possessing different values and a different major carrier (holes for the zig-zag direction and electrons for the armchair) [3, 10, 15]. The values for mobility and effective carrier masses are extremely sensitive to the number of layers [10] and are predicted to vary greatly from the monolayer to the bulk form [15]. Nevertheless, for samples of thickness on the order of a few nm to a few dozen nm, hole hall mobility was determined to be around 600 $cm^2V^{-1}s^{-1}$ at room temperature and up to 1,000 $cm^2V^{-1}s^{-1}$ at 120 K along the armchair direction, while bulk black phosphorus reaches values of 1,000 $cm^2V^{-1}s^{-1}$ at ambient temperature and up to 55,000 $cm^2V^{-1}s^{-1}$ at 30 K. In these conditions, electron mobility is 1,000 $cm^2V^{-1}s^{-1}$ and 10,000 $cm^2V^{-1}s^{-1}$ [14].

The same authors measured the on-off ratio of thin black phosphorus films transistors, obtaining values ranging from 10^3 to 10^5, depending on the film thickness [10–13]. The mobility/on-off ratio combination puts black phosphorus in a region of the mobility/on-off ratio space (Figure 1.5) not easily covered by the TMDC, nor by graphene. The combination of simultaneously high mobility and high on/off ratio renders black phosphorus in a prime position for applications in high-frequency and high-speed electronics [3].

Another interesting transport property is the effective mass of holes and electrons

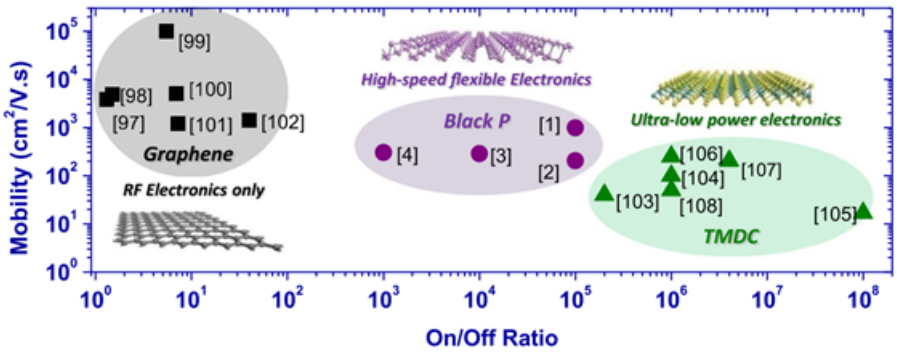

Figure 1.5: Mobility/on-off ratio spectrum of 2D-nanomaterials, spanning the graphene region (black squares and black region), the black phosphorus region (purple dots and region) and the transition metal dichalcogenides (green triangles and region). Numbers represents the references at the source material. Adapted from reference [3].

that are about 10 times greater in the zig-zag direction, than in the armchair for any given thickness [15]. Extraordinarily, for a monolayer phosphorene, it's predicted that the hole effective mass is 42 times higher in the zig-zag than in the armchair direction [15].

Moreover, on top of the advantages black phosphorus presents over its 2D counterparts, its most exciting feature is its in-plane anisotropic behavior [5, 11, 15–18], hinted above by the carrier mobility. Also present in other lesser-known TMDCs, the ability to respond differently to stimulus applied in different in-plane directions grants opportunities for unforeseen devices and applications [3]. The anisotropy extends to optical [11, 15, 19, 20], electronic [5, 11, 12, 15], phonon [11, 17] and thermal [16, 21] properties.

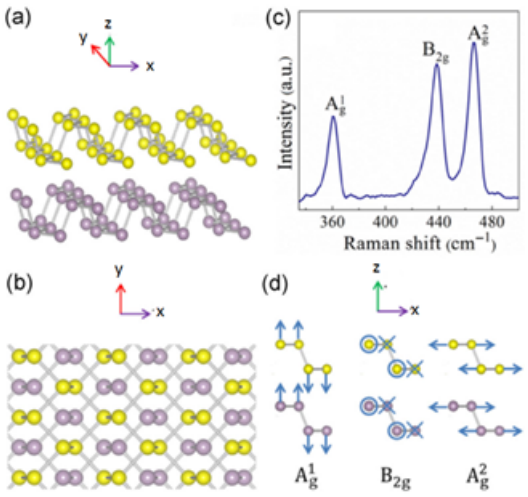

Figure 1.6: a) Perspective and (b) top views of 2 layers of black phosphorus. c) Typical Raman spectra of BP. d) Schematic diagram of atomic displacements of the phonon modes. Adapted from reference [17].

Figure 1.6-d displays the different phonon modes present in the black phosphorus crystal structure. The A_g^1 mode is sensitive to uniaxial strain in the armchair direction, while the other two modes (A_g^2 and B_g^2) are sensitive to strain induced in the zig-zag direction. Therefore,

black phosphorus presents an anisotropic mechanical response to uniaxial strain [17].

When illuminated by a plane-polarized light, black phosphorus is shown to respond differently depending on the angle between one of the in-plane directions and the light polarization . This is evidenced by Figure 1.7-a, where by Raman spectroscopy one can see that the predominant A_g^2 vibration mode peak decreases its intensity as the angle between the excitation light polarization and the armchair direction (x) increases. This anisotropy will also be present in other forms of interaction between polarized light (including circular polarized) and the surface of black phosphorus, such as photoluminescence [11, 19, 20]. This remarkable feature of black phosphorus can be used to create novel optoelectronics device [3].

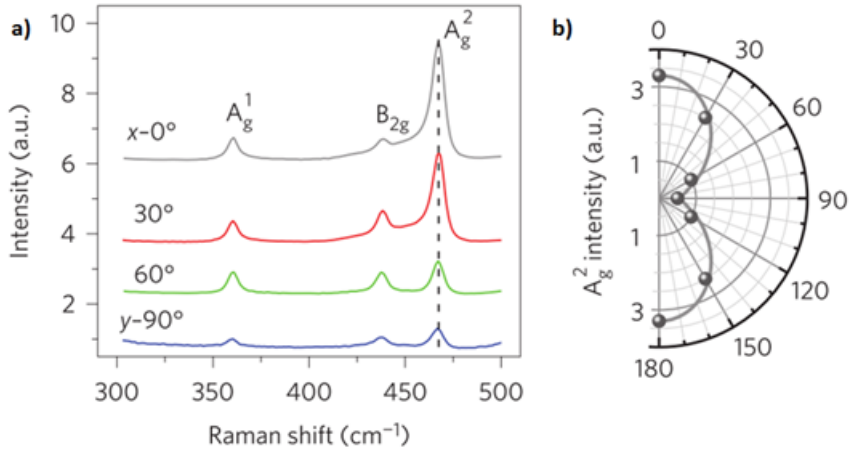

Figure 1.7: a) Raman spectra of black phosphorus with different angles between the excitation light linear polarization and the armchair direction (x). b) Angular plot of the A_g^2 vibration mode as a function of this angle, with a $\cos\theta^2$ function fit. Adapted from reference [20].

It was also reported that black phosphorus presents an anisotropic heat transfer, with a preferred axis for heat transport (zig-zag direction, Figure 1.8-a), which is orthogonal to the preferred electron transport direction (armchair) [16, 21]. Therefore, black phosphorus becomes a viable option for applications in thermoelectric devices reaching commercially viable energy conversion efficiencies [21, 22]. This is also evidenced by the different coefficients of absorptivity, reflectivity and transmissivity of light for the two in-plane directions (Figure 1.8-b) [16].

This subchapter of the introduction concerning black phosphorus and its astounding properties just scratches the surface of interesting physics and material science that can be done using this material. Even new physics is being performed in phosphorene, such as negative Poisson ratio [23] and electronic correlations at extreme conditions [24, 25]. Furthermore, many applications for phosphorene have already been proposed such as in high frequency electronics and optoelectronics [10, 13], photocatalysis [6], photovoltaics [26], catalysis, cancer therapy [27] and sensors [28].

On the other hand, synthesizing black phosphorus has been a cumbersome task on its own, specially trying to create thin films and the monolayer phosphorene [30]. Currently,

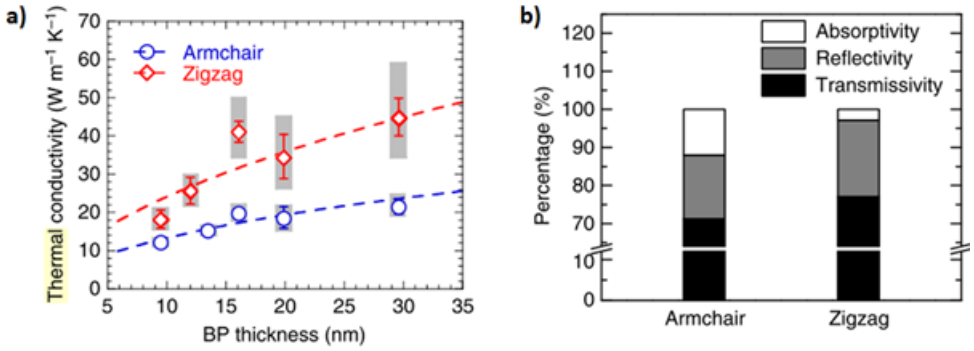

Figure 1.8: a) Thermal conductivity in both in-plane directions of black phosphorus as a function of thickness. b) Coefficients of absorptivity, reflectivity and transmissivity of the in-plane directions of black phosphorus. Adapted from reference [16].

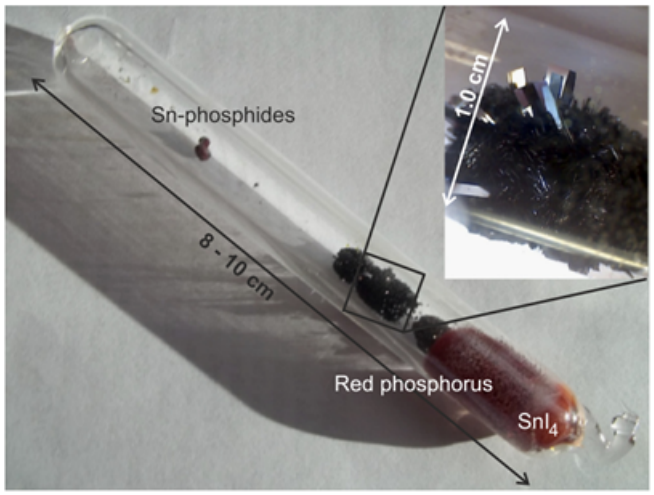

Figure 1.9: Silica ampoule after the synthesis of Black Phosphorus (image inlet) with reminiscent red phosphorus, SnI4 and Sn-phosphides. Adapted from reference [29].

the main techniques regarding BP growth are:

- High-pressure and high-temperature (HPHT), where white phosphorus or red phosphorus are subjected to temperatures and pressures of up to 800 ^{o}C and 4.5 GPa, respectively [31].
- High energy mechanical milling (HEMM), where amorphous red phosphorus is subject to a ball mill, where the temperature and pressure reaches values of 200 ^{o}C and 6 GPa, respectively [32].
- Mineralizer-assisted gas-phase transformation (MPGT), where amorphous red phosphorus is heated up to 500 ^{o}C along with Sn/SnI4 as a mineralization additive. Black phosphorus is then directly formed during the cooling of the gas-phase (Figure 1.9) [29].

Despite these methods creating crystals of several millimeters and high crystalline quality and purity, they are indirect ways of obtaining monolayer or thin films of phosphorene

[30, 33]. Currently, the scarce methods to obtain few-layers phosphorene are mostly restricted to thermal deposition [30], mechanical cleaving [33] and liquid-exfoliation [34]. Although more efficient methods aiming large-scale production are still under research [3].

1.2 Black Phosphorus Ambient Instability

Even though black phosphorus is the most thermodynamically and chemically stable allotrope of phosphorus, it is prone to oxidation [35–37]. Temporal evaluation of black phosphorus field effect transistors exposed to the environment showed that this oxidation was accompanied by a degradation of the electronic properties [13, 38] and roughing of the surface [39].

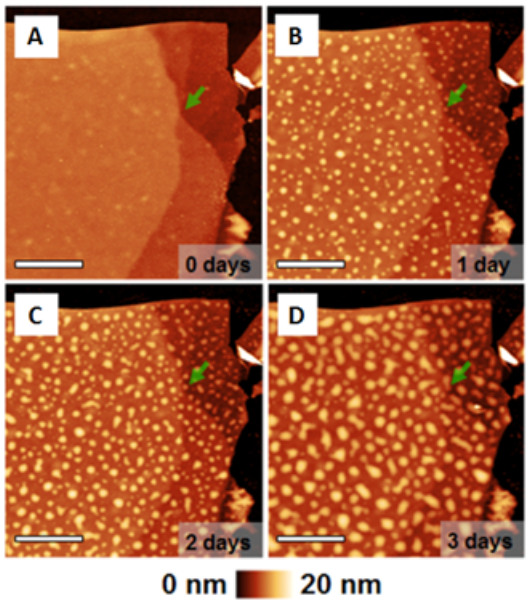

Figure 1.10: AFM height images of a black phosphorus sample under ambient conditions after exfoliation (a), after 1 day exposure (b), 2 days exposure (c) and 3 days exposure (d). The green arrow points to the same spot in every image. As the time goes, blisters form on the surface of the crystal. Scale bars are 1µm. Adapted from reference [38].

Figure 1.10 shows the temporal evolution of AFM height images of a black phosphorus crystal exposed to the environment. Note that, as time goes, blisters begin to develop atop the crystal and grow. These blisters are believed to be phosphoric acid bubbles, as suggested by XPS measurements [38]. This oxidation leads to almost complete degradation of black phosphorus flakes [33, 40], as is evidenced in Figure 1.11, that shows optical microscopy images of a flake exposed to the environment for several days. On the other hand, an early work reported that if the crystal is exfoliated under an inert atmosphere of dry nitrogen, no oxidation occurs [41]. The oxidation will also not occur when black phosphorus is not exposed to light [37], or if solely exposed to a mixture of water and oxygen [37]. Therefore, the main factors contributing to this oxidation are believed to be water, oxygen and light altogether [37].

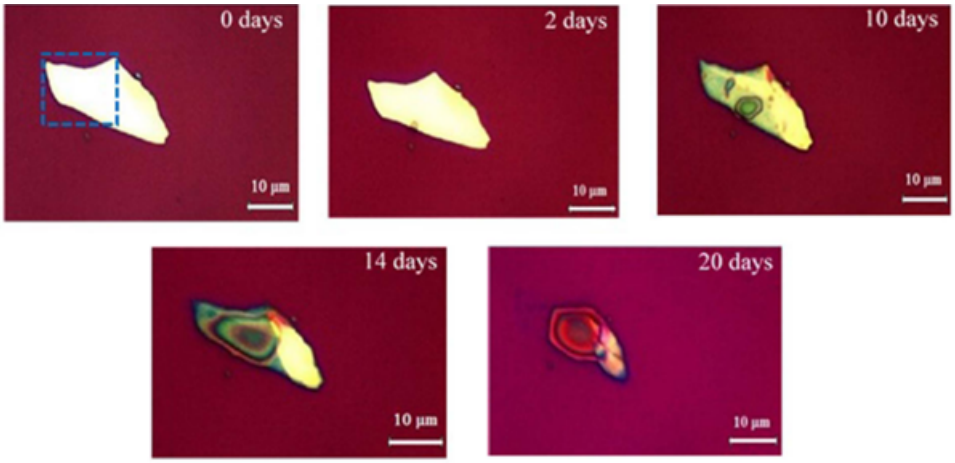

Figure 1.11: Optical microscopy images of a black phosphorus flake after exfoliation (0 days), and after 2, 10, 14 and 20 days exposed to the environment. Adapted from reference [38].

The etching of the flake is due to the oxidation of the surface, followed by the formation of phosphoric acid, that subsequently evaporates exposing the layers underneath [40]. This degradation is currently the prime factor preventing further development and application of phosphorene-based electronic devices, and is viewed as one of the key subjects to be further researched [3, 37, 42]. Hence, this project aims at answering some of the questions concerning this oxidation and hope to help overcoming this barrier.

Early approaches to circumvent this problem have been the passivation of the surface. This passivation can be done by several methods, such as encapsulation by dielectrics, polymers or molecules [38, 43], covalent functionalization [44] or doping [45]. However, some of these methods are believed to decrease the mobility of carriers and have an overall downgrade effect of the electronic properties [44, 45]. Moreover, some of these encapsulations methods are also susceptible to penetration over time by oxygen and water in the interface due to weak intermolecular forces, eventually leading to degradation [43]. Fortunately, if grown in a controlled manner, the native oxide of phosphorene could be used as an protective layer or a functional material on its own, leading to a complementary advantage of black phosphorus over other 2D materials [46]. An example of the success of such method is the triumph of silicon over germanium due to the silicon oxide controllable thermal growth, opposed to the hardly controlled germanium oxide growth, amongst other factors.

1.3 Early studies of the oxidation

In light of such need for understanding the mechanism of oxidation of phosphorene, an early work by Favron *et al.* has been performed using mainly Raman spectroscopy and has given the first insights about such mechanism [37]. At first, they started exfoliating phosphorene sheets at ambient conditions and taking images using atomic force microscope (AFM).

In agreement to previous studies [13, 33, 38, 47], when phosphorene was exfoliated

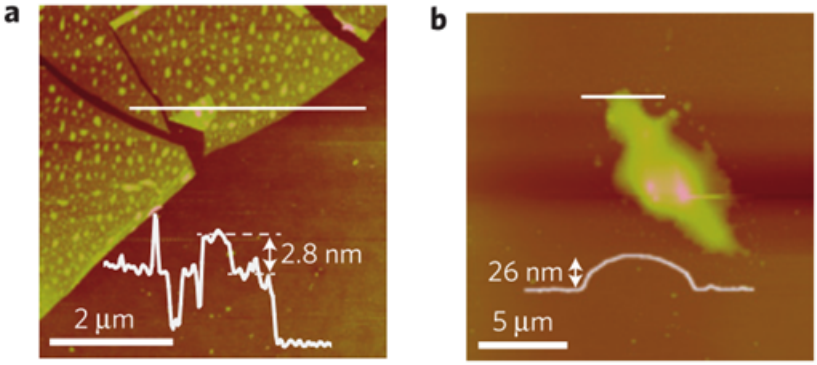

Figure 1.12: AFM images of a phosphorene sheet over a SiO_2/Si substrate immediately after exfoliation under ambient conditions (a) and after a few days (b). Adapted from reference [37].

in ambient conditions, uniformly distributed bumps appeared on its surface (Figure 2.12-a), suggesting that a nucleation step is required. These bumps sometimes exceed even the flake's thickness. As time passes, these bumps grow and transcends into bubbles across the surface of the flake (Figure 1.12-b)[37]. These bubbles are believed to be phosphoric acid in the final step of the degradation process [37, 47]. This degradation and formation of bumps and bubbles was not observed in samples that were kept in the dark, suggesting that this in fact, a photo-oxidation process [37]. Recent theoretical work, however, disputes this statement showing results that water could in fact facilitate this oxidation to occur in the dark [48].

Favron *et al.* continued the investigation by measuring Raman shift of a black phosphorus flake exposed to ambient environment repeatedly over a period of time (Figure 1.13-a), note that the black phosphorus modes decay rapidly, showing complete degradation of the atomic structure.

Furthermore, to evaluate the role of water and oxygen in the oxidation, they exposed a freshly cleaved 20 nm phosphorene crystal to a mixture of oxygen and water and followed the quenching of the A_g^2 mode (Figure 1.13-b). This experiment was also repeated while exposing a cleaved crystal to vacuum (<6.6x10^{-9} bar), air and to air while been encapsulated under a 300 nm layer of parylene polymer cap used as a moisture barrier. The laser probe fluence varies through these measurements.

Under air or water-oxygen mixture, the attenuation of the Raman mode is exponentially dependent on time. The faster decay for the air measurements is due to the increased laser fluence. At the vacuum and parylene cap measurements, there was no significant decrease in the mode intensity other than the normal fluctuations. Subsequently, to better understand the light influence over the degradation, black phosphorus flakes (8 nm) were submerged in an aqueous solution and illuminated with different laser fluences and the normalized Raman intensity was measured through time (Figure 1.14-c). As the laser fluence was increased gradually from 1.2x10^4Wcm^{-2} to 6.4x10^4Wcm^{-2}, the decay constant is gradually increased, with sharper quenching of the intensity for higher fluences. These experiments helped to define oxygen, water and light as major factors of the oxidation and degradation of black phosphorus [37].

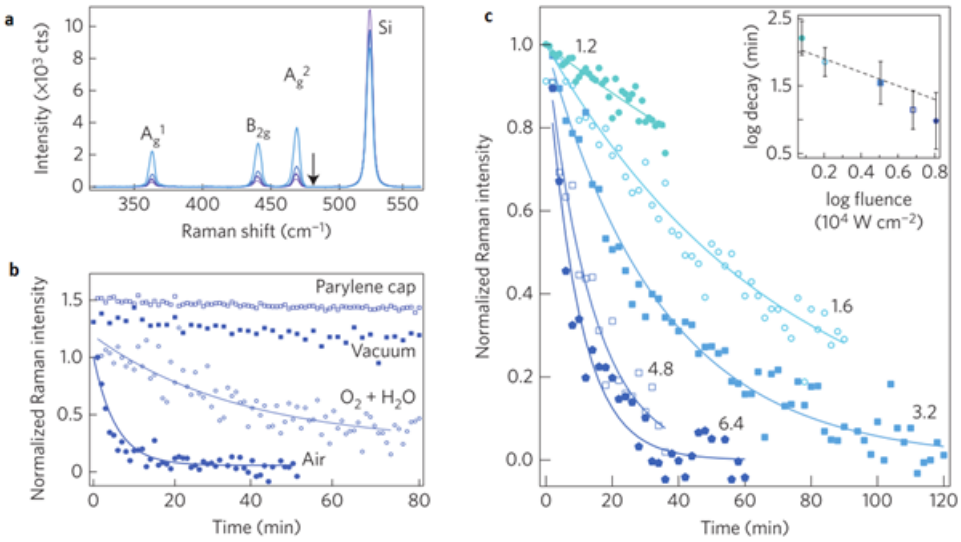

Figure 1.13: (a) Raman spectra at λ=520 nm on a 5 nm thick sample measured at ambient conditions at 24, 48, 96 and 120 min after cleavage. (b) Time dependence of the A_g^2 Raman mode of a black phosphorus flake over time under different conditions (note that the air and O_2+H_2O have different decay rates due to the higher laser fluence used in the air measurement). (c) Time evolution of the A_g^2 Raman mode of a 8 nm thick black phosphorus sample immersed in aqueous solution under air for different laser fluences. Inset: Log-log plot of the decay time by the laser fluence. Adapted from reference [37].

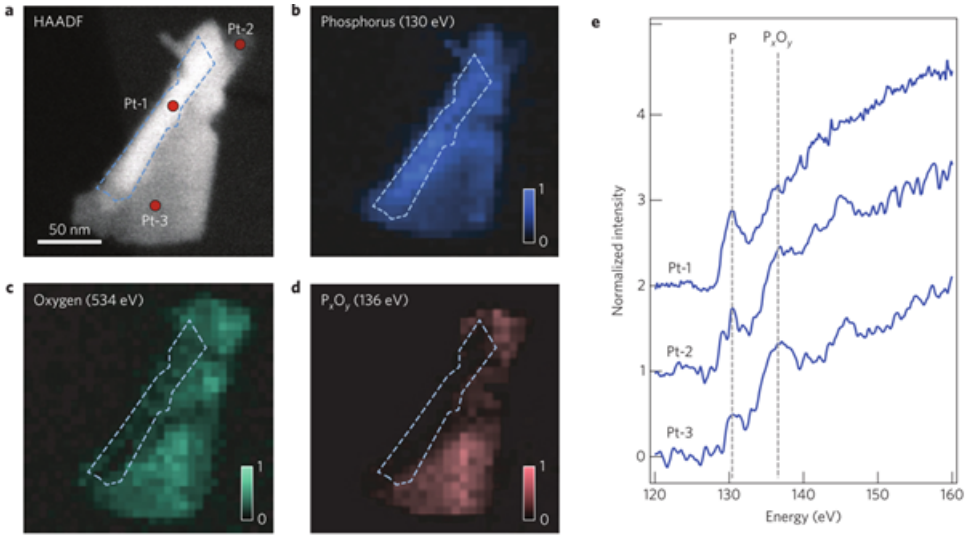

Figure 1.14: Chemical analysis performed by transmission electron microscope electron energy loss spectroscopy (TEM-EELS) of a phosphorene flake exfoliated under ambient conditions and light. With different regions with approximately 7 layers (Pt. 1), 2-3 layers (Pt. 2 and 3). (a) High-angle annular dark field contrast image taken at 80 kV. EELS image of the flake highlighting the phosphorus (b), oxygen (c) and P_xO_y (d) peaks. (e) EELS spectra corresponding to the different regions at (a). Adapted from reference [37].

They also performed electron energy loss spectroscopy (EELS) of a black phosphorus flake recently cleaved at ambient air and light, to underscore how the number of layers affects the oxidation process. The number of layers was defined by high-angle annular dark

field (HAADF) on a transmission electronic microscope (TEM) (Figure 1.14-a). 3 distinctive regions are visible with approximately 7 layers (Pt. 1) and 2-3 layers (Pt. 2-3). Using TEM-EELS, images of the distribution of black phosphorus, oxygen and phosphorene oxide (P_xO_y) were obtained (Figures 1.14-b-d, respectively). The EELS spectra for the different regions are also given (Figure 1.14-e). The thicker regions presents little to no oxidation, while the thinner regions presents almost full oxidation. It was possible to conclude that oxidation susceptibility is indirectly proportional to the number of layers [37]. This is further corroborated by theoretical calculations [49].

Complementary to Favron et al. , other authors reported results that indicated strong evidences that water, by itself, do not oxidize black phosphorus. These results come from different experiments of x-ray photoelectron spectroscopy [50], optical micrograph [51], Raman spectroscopy [52] and nuclear magnetic resonance spectroscopy [53]. This is further corroborated by successful exfoliation of black phosphorus nanosheets on deoxygenated water [34, 54].

Chapter 2

Materials and Methods

2.1 Black Phosphorus Crystals

Four crystals of black phosphorus of approximately 1x1 cm were acquired from the supplier HqGraphene with a purity of >99.995%. The samples were stored in inert nitrogen atmosphere before being used due to its instability. Clean surfaces of black phosphorus were produced by mechanical exfoliation using a scotch tape in vacuum. Typically, after 2-3 exfoliations, the surface presented only trace amounts of carbon and oxygen.

2.2 X-ray photoemission spectroscopy

X-ray photoemission spectroscopy, commonly referred to by the acronym XPS, and also known as electron spectroscopy for chemical analysis (ESCA), is an experimental technique based upon the photoelectric effect that mainly probes the elemental composition, stoichiometry, chemical and electronic state of a given sample. It is quantitative and surface-sensitive.

In the photoelectric effect, a photon ($h\nu$) interact with an electron (e^-) and transmit energy to it. If this energy is enough, the electron may be excited from an initial energy state (E_i) to a final state with energy higher than the ionization potential of the atom (E_f), travel through the material towards the surface ($z = 0$) and finally, transmit through it towards the vacuum. When this happens, we say the electron has been photo-emitted and thus is now a photoelectron [55]. This process is sketched in Figure 2.1.

The kinetic energy (KE) of the photo-emitted electron is the energy leftover on the electron after the photoemission process. Therefore, this energy is defined as being the difference between the photon energy ($h\nu$) and the sum of the electron's binding energy (BE) and the material's work function (ϕ). Binding energy is the energy required to release an electron from the atom, which is derived from the electromagnetic interaction between the electrons and the nucleus, and the work function is the energy required to transmit the electron from the

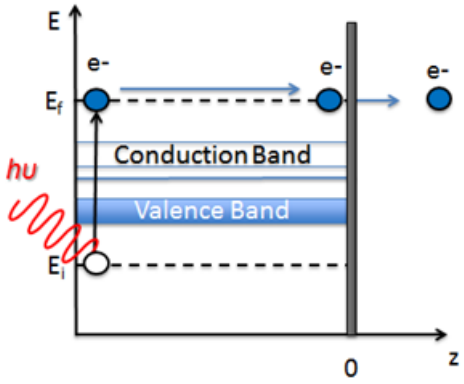

Figure 2.1: Scheme of the photoemission process, where an electron (e-) is photo-excited by a photon ($h\nu$) from an initial state (E_i) to a final state (E_f). The electron then propagates through the material towards the surface ($z = 0$) and cross it to the vacuum.

material's surface to the vacuum. This energy balance is summarized in Equation 2.1.

$$KE = h\nu - BE - \phi \tag{2.1}$$

The binding energy of an electron is directly proportional to the effective potential it is submitted to. This potential in its turn is sensitive to the atom's atomic number and oxidation state. Given the dependency of the kinetic energy to the binding energy, the photo-emitted electron will carry information about the element, its chemical state and local surrounding.

The typical experimental setup for a XPS experiment is shown in Figure 2.2. Where an X-ray source, that could be an X-ray tube or, in our case, a synchrotron accelerator, emits photons into the surface of a given sample. The common photon energies for a XPS experiment are from 100-2000 eV. This way, the outgoing electrons will have low kinetic energies, therefore, only the electrons created close to the surface will be able to reach the detector, due to strong inelastic scattering. The sample will start to emit photoelectrons that subsequently are collected by a hemispherical analyzer. In the analyzer, electrons will have to pass through a semi-circular trajectory towards the detector. The electric field applied in-between the hemispherical shells will determine the electron's energy within a certain acceptance, set by the pass energy (ΔE); the smaller the ΔE the better spectral resolution, lower signal intensity and higher collection time. The photoelectrons will reach the detector and will be counted. Most setup must work in ultra-high vacuum environment to minimize the electron losses to scattering in the gases.

Moreover, this experiment will have as an outcome data a spectrum of electron counts as function of the kinetic energy. As a convention, the kinetic energy will be converted to binding energy for a better interpretation. In order to faithfully convert these values we need to use the work function. The work function of the sample (ϕ_S) is unknown and would be hard to determine, requiring a set of experiments designed specifically for that purpose. Such task is cumbersome and there is an easy way around it. During the commissioning of the

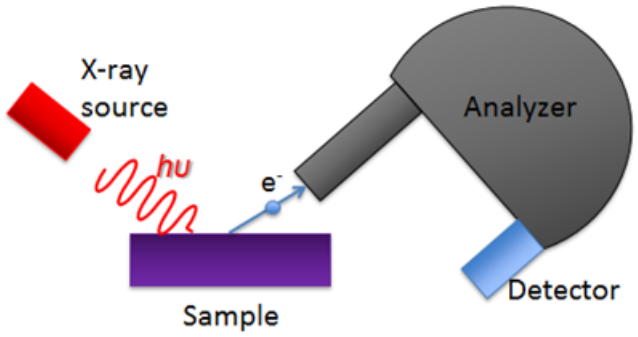

Figure 2.2: Typical experimental setup of a XPS experiment, where an X-ray source emits photons into a sample. The photoelectrons are then collected by a hemispherical analyser and counted in the detector.

hemispherical analyzer, it is determined the analyzer's work function (ϕ_{ana}). By connecting the sample electrically to the analyzer, we align their Fermi levels. As a consequence of energy conservation, the sum of the kinetic energy of the electron in the material (E_{KE}) and ϕ_S is now equal to the sum of the kinetic energy detected in the analyzer ($E_{KE,meas.}$) and ϕ_{ana}. Since ϕ_{ana} is known, it is now possible to directly convert the kinetic energy to binding energy. This procedure is exemplified in Figure 2.3.

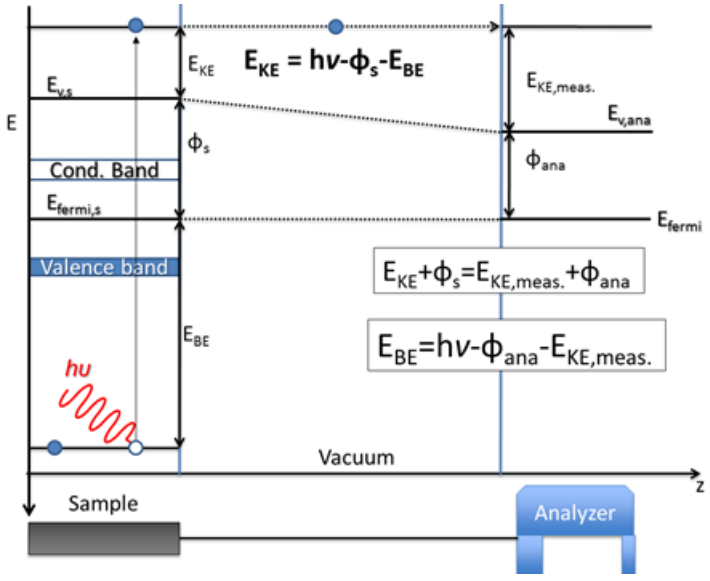

Figure 2.3: Energy diagram where the electron photo-emitted from the atom travels through the vacuum towards the analyser, and have its kinetic energy measured. The sample and the analyzer are electrically connected, aligning their fermi levels.

A typical XPS spectrum is illustrated in Figure 2.4. The orbitals of each element present in the sample with binding energy lower than the photon energy will appear in the spectrum as peak. The valence orbitals will be cluttered together near the end of the spectrum, close to the binding energy of 0 eV, whilst the core-orbitals will be more scattered through the spectrum and more easily identified. The p, d and f orbitals appear as doublet, as consequence of

the spin-orbit coupling that breaks the degeneracy of the states. Photoelectrons that manage to leave the surface of the materials but have suffered energy losses through several inelastic scattering processes are represented in the spectrum as a background signal. Secondary electrons created by the inelastic scattering also contributes to the background. This background needs to be accounted for when quantifying the spectra. The methodology for the quantification of the peaks is described in appendix A.

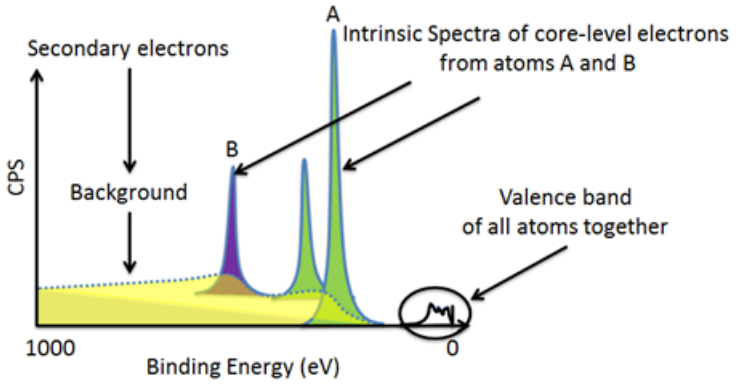

Figure 2.4: Typical XPS spectrum. Where we have intrinsic peaks attributed to orbitals of atoms A and B. Where the A atom's orbital is subject to spin-orbit coupling, hence the double peaks. It is present also the background (secondary electrons) e the valence band of all atoms probed.

The intensities of the intrinsic peaks of the core-level electrons are proportional to various factors, amongst them are the photon flux ($F(h\nu)$), the number of atoms of determined element being irradiated (N), the photo-ionization cross section ($\sigma(h\nu)$) and the total transmission of the analyzer for the electron kinetic energy ($T(KE)$). This dependence is described in Equation 2.2.

$$I_0 \approx F(h\nu) * N * \sigma(h\nu) * T(KE) \tag{2.2}$$

The probability of a photon interacting with an atom's electron is governed by the effective photoemission cross-section (σ). This factor depends on the atomic number of the absorbing element, the electron's orbital, the photon energy ($h\nu$) and the asymmetry coefficient ($L_a(\gamma)$) of the orbital, where γ is the angle between the incoming photon and the outgoing electron. For example, the s orbital is a sphere possessing complete symmetrical shape; therefore its asymmetry coefficient is 1. That's not the case for p orbitals, where this coefficient has a complex angular dependence, as illustrated in Figure 2.5.

Thus, one needs to take into account the asymmetry of the orbitals during the data analysis. However, there is an angle between the photon incidence and the electron detection, in which the effects of ($L_a(\gamma)$) is minimized, reaching a point where it is less important than many other factors. This angle, called magic angle, is $\gamma = 54.7°$. If in a XPS experiment the angle between the analyzer entrance and the incoming photons is the magic angle, there is no need to worry about the asymmetry of photo-emission process.

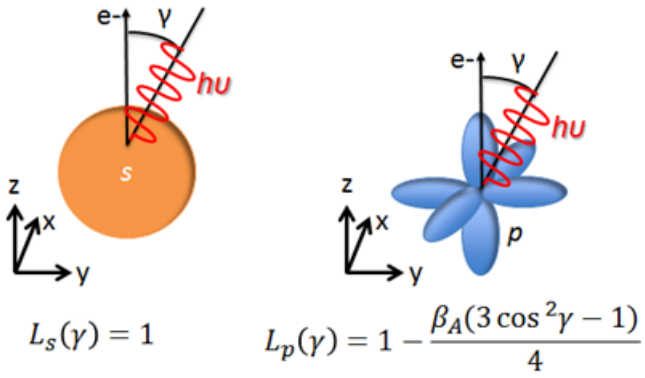

Figure 2.5: Asymmetry parameters for s and p orbitals. Where γ is the angle between the incoming photon ($h\nu$) and the outgoing electron (e^-) and β_a is a constant of the orbital.

It is clear from equation 2.2 that integrated intensities cannot be used directly to determine elemental concentrations. One has to account for the different factors composing the intensities. An overview of how to compare different elements composition and draw the stoichiometry of a structure is summarized in appendix B.

Since we are using a range of photon energies of 100-2000 eV, and most core-electrons have binding energies on the same order of magnitude, the photo-emitted electrons will present kinetic energies of 0-1500 eV. In accordance to the universal curve of inelastic mean free path or IMFP (λ) (Figure 2.6-a), electrons with these kinetic energies have an IMFP of about 0.4-5 nm. Therefore, most of the electrons reaching the analyzer will come from the very first layers. In fact, in Figure 2.6-b we can see that 65% of the electron signal of the XPS comes from electrons originating from depths shallower than λ, and about 95% of the signal from depths shallower than 3λ. Hence the surface sensitivity of this technique.

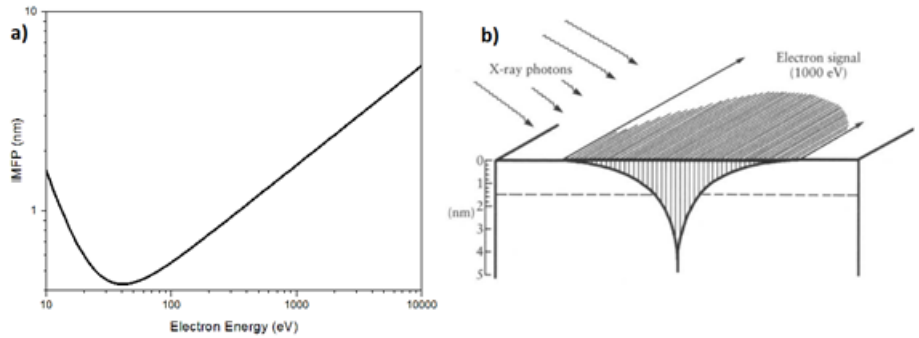

Figure 2.6: a) Universal inelastic mean free path (IMFP) curve by electron's kinetic energy. b) Signal intensity of electrons with 1000 eV of kinetic energy, as a function of depth. Dotted line corresponds to the attenuation distance or IMFP (λ). Adapted from reference [56].

Now taking into account the effects of attenuation, one can modify the signal intensity equation (Equation 2.2) to better represent the depth dependence. This is called the Beer-Lambert relation and is shown in Equation 2.3.

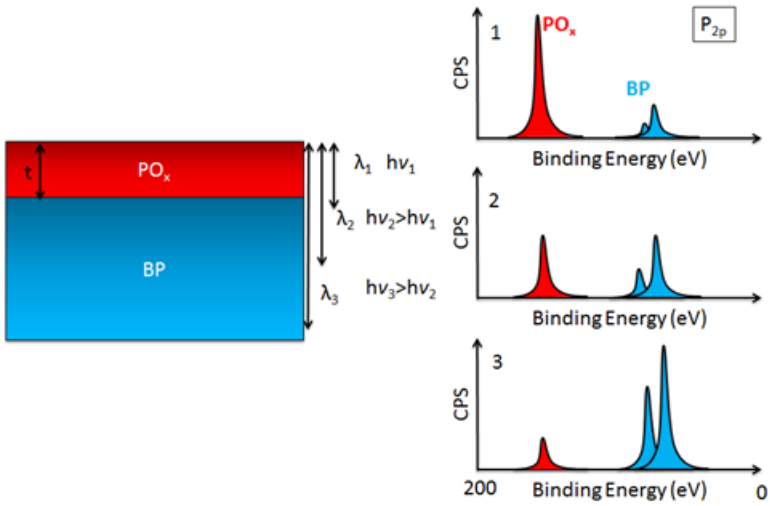

Figure 2.7: Imagining an oxide layer (PO_x) atop a black phosphorus crystal (BP) being shone by 3 different photon energies $h\nu 3 > h\nu 2 > h\nu 1$ with respective IMFP $\lambda 3 > \lambda 2 > \lambda 1$. Their XPS spectrum are represented to the right.

$$I = I_0 e^{\left(-\frac{\tau}{\lambda \cos\theta}\right)} \tag{2.3}$$

This equation illustrates the signal attenuation of electrons arising from depths greater than τ, with a emission angle of θ relative to the surface's normal, as according to Figure 2.8. Measurements of the intensity as function of the incidence angle or photon energy, which causes variations of λ, can be used to create a depth concentration profile. As an example, imagine there is an oxide layer of phosphorus (PO_X) of thickness τ grown atop a black phosphorus crystal (BP), shown in Figure 2.7. The ratio between the PO_X signal and the BP signal will be proportional to Equation 2.4.

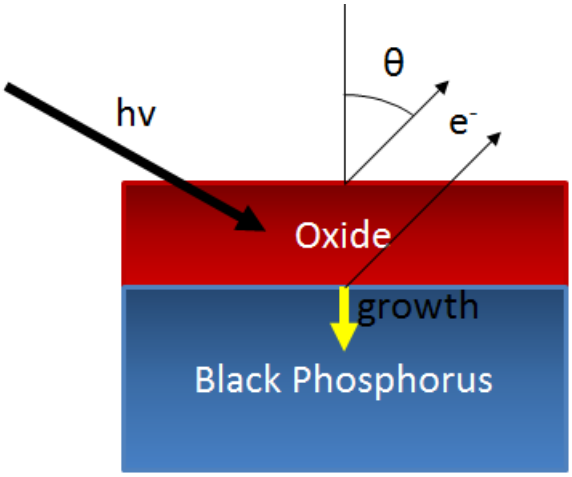

Figure 2.8: Image depicting the relevant factors of the Beer-Lambert equation.

$$\frac{I_{PO_x}}{I_{BP}} = \frac{I_{0POx}}{I_{0BP}} e^{\left(\frac{\tau}{\lambda \cos\theta} - 1\right)} \tag{2.4}$$

Therefore, it is possible to obtain points of this ratio by changing the incidence angle (when working with an X-ray tube) or the photon energy (when working with a synchrotron). By fitting an exponential curve to the measured points, it is possible to determine the oxide layer thickness.

The possibility to perform measurements with variable photon energy, also influences the quantification of the surface composition. Equation 2.2 indicates that to quantify spectra measured with a fixed photon energy, one needs to know the cross section and total transmission of the analyzer. On the other hand, if the photon energy can be varied in way to keep the kinetic energy constant, one need the cross section and the total photon flux. Although the total transmission can be measured experimentally, it is more cumbersome and sensitive to errors, than measuring photon flux.

2.3 Ambient Pressure X-ray Photoemission Spectroscopy

The main technique used in this project is the ambient pressure X-ray photoemission spectroscopy (AP-XPS). This technique follows the same principles the XPS previously described, but the experiments are performed with the sample under pressures in the order of a few mbar.

To keep the detector under UHV conditions, a multi-stage differential pumping system is inserted between the experimental chamber and the analyzer, in a manner that the pressure decreases gradually after each stage, until the pressure difference between the analyzer and the experimental chamber is in the order of 10^6 to 10^8. This is shown at Figure 2.9.

The small apertures in the millimeter range separated by several centimeters reduce drastically the collection of photoelectrons due to the extreme reduction in the solid angle seen by the analyzer. In order to compensate this loss, modern spectrometers have a set of electrostatic lenses that focuses the electrons on each aperture, hence considerably increasing the overall collection efficiency of the analyzer.

To further minimize the signal loss due to electron scattering in the gas before inside the chamber , the sample is mounted extremely close to the first aperture of the differential pumping, at a distance of the same order of the aperture's diameter (R$\approx$0.1-1mm). This enables the electrons to travel the least path possible through the gas, while the pressure just above the sample's surface is still 95% of the pressure of the chamber [57, 58].

The experiments were performed in a synchrotron based AP-XPS endstation at the TEMPO beamline of the synchrotron SOLEIL[59]. Throughout all measurements, the samples were at room temperature. The black phosphorus crystals were cleaved in high vacuum at pressures around 10^{-8} mbar in the load lock. Subsequently, the cleaved samples were transfered to the experimental chamber with a base pressure of 10^{-9} before any gas introduction

For most experiments, we first measured a wide energy survey at low energy resolution (30 eV pass energy) and detailed high resolution spectra (10 eV pass energy) for the

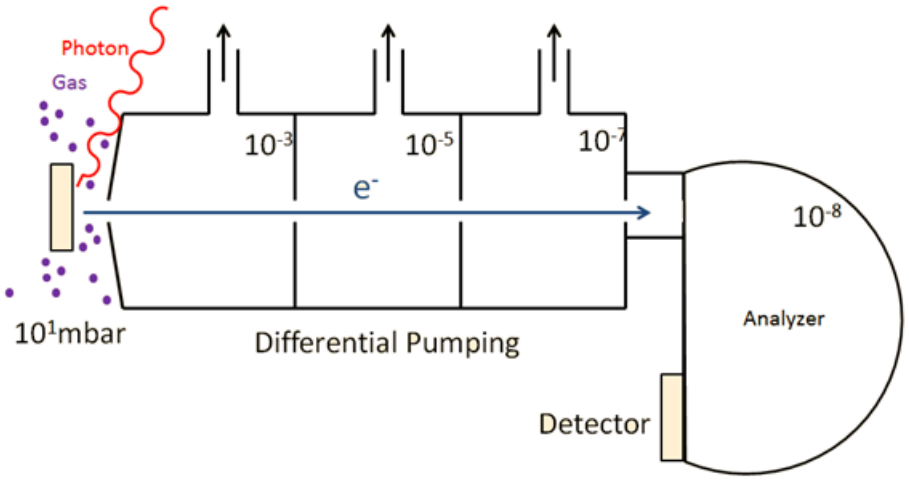

Figure 2.9: Experimental apparatus of an AP-XPS.

phosphorus 2p, oxygen 1s and carbon 1s regions. The incoming photon energy for these regions were 330 eV, 530 eV and 480 eV, respectively. Thus, all the outgoing electrons have approximately the same kinetic energy of 200 eV and consequently, the same total analyzer transmission. The photon beamspot size was 0.1 x 0.1 mm.

Thereafter, we submitted the samples to pure O_2, pure H_2O or a mixed O_2 + H_2O atmospheres at pressures in the order of 1-10 mbar. During the exposition, that normally lasted from 1.5 to 3 hours, we measured several low resolution fast spectra (aprox. 2 min per spectra) at fixed photon energy to follow the surface kinetics.

Finally, after the removal of the gas atmosphere we measured high resolution spectra under high vacuum conditions, with the same parameters as before the oxidation.

2.4 DFT Calculations

Calculations were performed with the Quantum ESPRESSO package [60] using the Perdew, Burke, and Ernzerhof (PBE) exchange and correlation potential [61] and the exchange-hole dipole moment (XDM) [62, 63] dispersion correction. Projector augmented wave (PAW) potentials were taken from the PS library [64] and we employed a kinetic energy (charge density) cutoff of 70 Ry (700 Ry). The Phosphorene oxide was modeled as an overlayer on top of 5 layers of black phosphorus slabs separated by 15 of vacuum with the bottom two layers were held fixed at their computed bulk values. A k-point mesh equivalent to at least (12x12) for the (1x1) surface-unit-cell was used with Marzari–Vanderbilt cold smearing and a smearing parameter of 0.01 Ry. Core level shifts were computed with the DSCF (Self Consistent Field) method to capture both initial and final state effects [65].

Chapter 3

Results and discussion

3.1 Gas interactions

According to the literature [37, 42], light is the driving force for the oxidation of black phosphorus; supposedly promoting water and oxygen to react with the surface. On preliminary experiments we evaluated whether oxidation would occur if the black phosphorus crystal was exposed to an oxygen atmosphere with or without X-rays. When exposed solely to oxygen in the dark, XPS spectra measured afterwards revealed that there was no oxidation. Furthermore, when XPS measurements were performed whilst exposing the crystal to oxygen; oxidation took place. Therefore, we concluded that X-ray beams could also promote the oxidation; thus, there was no need to use an external laser light source. Our next experiments were then elaborated to evaluate the influence of such factors (light, water and oxygen) by varying X-ray beam time and gas atmosphere composition and pressure.

Initially, to assess if water, by itself, can oxidize the black phosphorus surface, we performed an experiment exposing a freshly in-vacuum cleaved flake to an atmosphere of 0.25 mbar oxygen-free H_2O. We obtained high resolution XPS spectra of the P_{2p}, O_{1s} and C_{1s} regions before the introduction of the atmosphere. Thereafter, we increased the pass energy (ΔE) and decreased the acquisition time to better follow the kinetics, subsequently introducing the H_2O atmosphere and shining the sample with a 730 eV photon beam. We followed the evolution of the aforementioned regions for a period of approximately two and a half hours, and the spectra are shown in Figure 3.1-a,b.

Evolution of the O_{1s} spectrum shown at Figure 3.1-b shows the rise of three features assigned to the H_2O in gaseous state (535.4 eV), H_2O adsorbed on the surface (532 eV) and adsorbed OH^- species (529 eV). The peaks' assignment was done based on several studies of the literature concerning water adsorption on the surface of metals and oxides [56, 66]. On the other hand, the P_{2p} spectral region on Figure 3.1-a shows a single doublet peak assigned as P bonded to other P atoms in pristine black phosphorus (130 eV), labeled as P-P. This feature is merely attenuated during the experiment. However, this attenuation is not due to oxidation,

since there are no additional peaks in the P 2p spectrum that could be assigned to phosphorus in other oxidation states. Instead, this attenuation is consistent with the electrons scattering on the adsorbed layer of water evidenced in the O_{1s} spectrum.

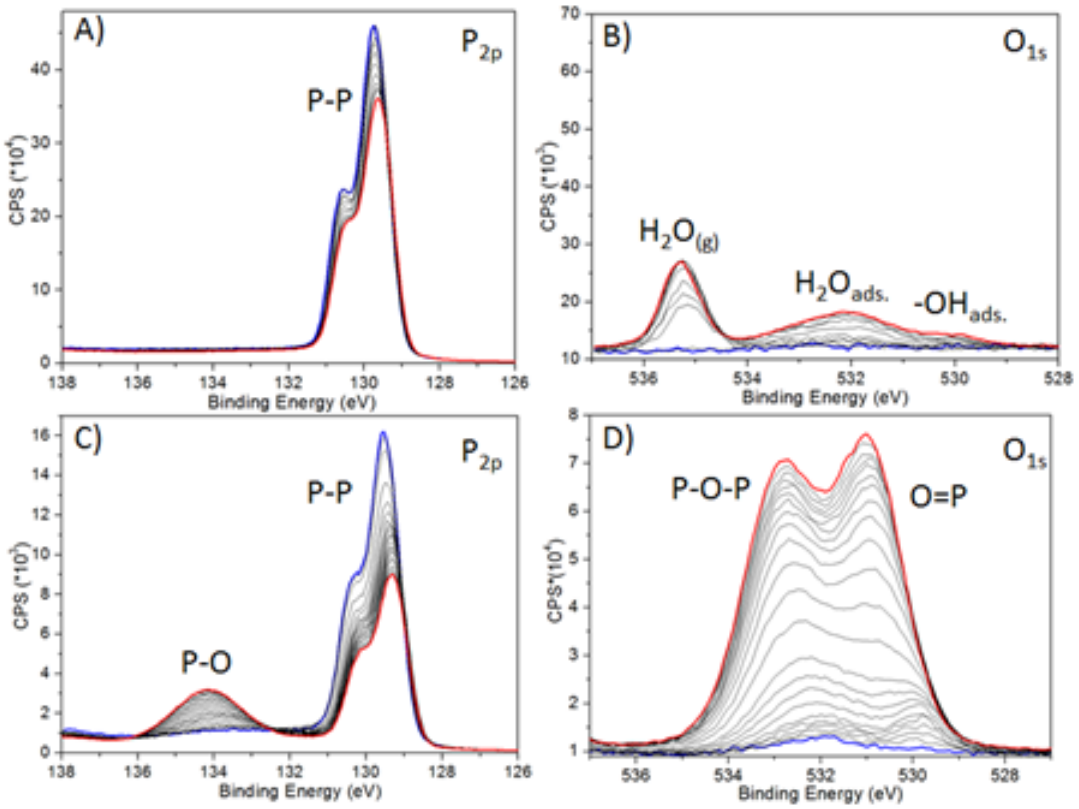

Figure 3.1: Evolution of the spectra regions P_{2p} and O_{1s} when exposing the freshly cleaved in-vacuum black phosphorus crystal to a 0.25 mbar H_2O oxygen-free atmosphere (**a** and **b**) and to a 1 mbar O_2 atmosphere (**c** and **d**). Thick blue line represents the first measurement, and the thick red line represents the last. Black lines represents intermediate spectra.

Finally, it is possible to conclude that black phosphorus do not oxidize solely exposed to water in our experimental conditions, that are equivalent to a relative humidity of approximately 1%. The resistance to oxidation in a H_2O atmosphere observed in our experiment agrees with other reports in the literature [53].

Sequentially, we cleaved the black phosphorus crystal in-vacuum and transfer it into the experimental chamber. We measured a XPS spectrum of the as cleaved sample to make sure the surface was clean. Afterwards we introduced an atmosphere of 1 mbar of dry O_2 and illuminated the sample with a 730 eV photon beam. Figure 3.1-c,d shows consecutive measurements of the P_{2p} and O_{1s} spectral regions for an exposure time of approximately 3 hours. We ran the experiment until there were no more visible changes in the spectra. In this experiment, we can observe in the P_{2p} spectra the clear development of an additional feature (labeled as P-O) at binding energy around 4 eV higher than the pristine black phosphorus peak's energy (P-P). This peak is assigned to phosphorus species in a different oxidation state. The O_{1s} region noticeably shows the rise of a spectral structure with two well defined peaks at 531 eV and 533 eV, indicat-

ing the formation of an oxide. The photoemission peaks related to O_2 gas are not shown here, appearing at a biding energy a few eV higher. In fact, phosphorus oxides normally presents 2 distinct oxygen species according to the literature [**Ziletti2014PhosphoreneOxidation**, 36], that can be attributed to these features. Therefore, we conclude that w the black phosphorus flake suffers superficial oxidation when exposed to a O_2 atmosphere of 1 mbar and in the presence of soft X-rays,

It is noteworthy that after about two and a half hour, the changes in the spectral features are minimal. This suggests that surface oxidation is somewhat limited, and may evidence that a passivation layer grew atop the black phosphorus flakes. We will return to this point in section 3.3, where we quantify the components as function of time to extract information about the reaction kinetics.

By also looking at the C_{1s} spectral region during the oxygen exposure experiment, one can see that the signal related to residual carbon species gradually decreases towards a near background level. Therefore, we can assume that during the oxidation of black phosphorus, these carbon species are also oxidized and eventually removed from the surface.

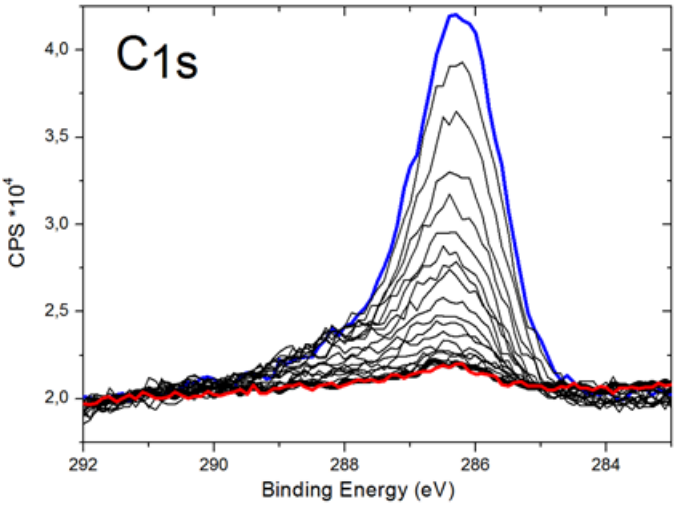

Figure 3.2: Evolution of the spectral region of carbon C_{1s} for a period of 3 hours during the 1 mbar O_{1s} atmosphere experiment. The thick blue line represents the first measurement and the red thick line represents the last measurement. Black lines represents intermediate steps of the evolution.

We evaluated the reproducibility of the limited oxide growth, by repeating the O_2 exposure experiment at variable pressures for freshly cleaved samples. For instance, in one experiment we exposed black phosphorus' flakes in oxygen atmospheres of up to 10 mbar for 3 hours. Nevertheless the pressure variations, the results are qualitatively the same. We observe ever smaller changes in the intensity as time increase suggesting a limited growth of the oxide layer.

For quantitative evaluation of the reproducibility, we fitted the P_{2p} spectra at the end of the O_2 oxidation experiments and compared the ratio of the areas of the peaks related to the

oxide and pristine BP. The fitting procedure is explained in Appendix A. Figure 3.3 shows an illustrative spectrum for P_{2p} region measured with a photon energy of 730 eV after exposing the surface of BP to 1 mbar O_2. The peak area ratio was 0.6:1 for a 730 eV photon energy, which was consistent across all the O_2 exposure experiments. This corroborates the hypothesis of a limited passivated layer, which, henceforth we refer as phosphorene oxide.

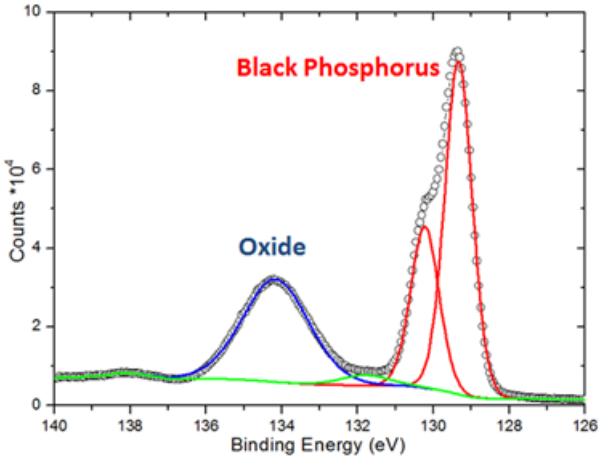

Figure 3.3: P_{2p} spectral region at the end of the oxidation with the oxide and black phosphorus peaks. Measured with a photon energy of 730 eV. Taken at the final of the 1 mbar O_2 experiment.

3.2 Oxide thickness

From our previous experiment, we identified that the oxide growth on the surface of black phosphorus under an oxygen atmosphere is kinetically limited. Furthermore, it is interesting to know the thickness of this oxide layer. In order to obtain this parameter we performed XPS depth profile experiments by measuring spectra at variable photon energies. We exposed a freshly cleaved black phosphorus flake to a 1-4 mbar O_2 atmosphere for a period of 1.5 hours under constant X-rays irradiation. Afterwards, we removed the O_2 atmosphere and measured high resolution XPS spectra with incident photon energies of 330 eV, 530 eV, 730 eV and 930 eV(Figure 3.4).

Figure 3.4 shows that as the photon energy increases, the ratio between the phosphorene oxide (134.1 eV) and pristine black phosphorus (130 eV) peaks diminishes. For higher photon energies, The P_{2p} region is measured with higher kinetic energy, which means a larger inelastic mean free path (λ) and consequently deeper probing depth as illustrated in Figure 2.6. Hence, we conclude that the oxidized and pristine phosphorus species are not homogeneously distributed in depth, but rather an oxide layer covers the pristine layers underneath.

To quantify the thickness of the surface oxide, we can assume a heterogeneous model where an oxide layer covers the entire surface of the black phosphorus crystal as illustrated in Figure 3.5. After fitting the spectra, we calculate the ratio between the areas of the

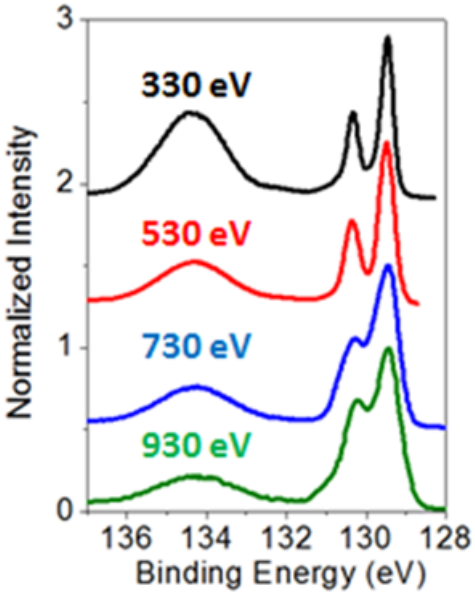

Figure 3.4: High resolution XPS spectra of P_{2p} region with different incident photon energies.

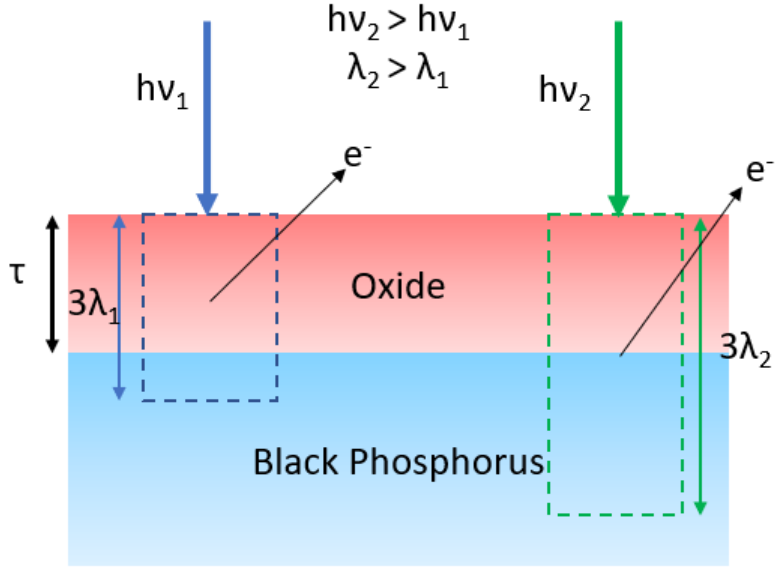

Figure 3.5: Model of the depth profile of a complete oxide layer at the surface of black phosphorus. With the incident photons ($h\nu$), outgoing electrons (e^-), inelastic mean free path (λ), probing depth (3λ) and oxide thickness (τ). By increasing the photon energy, we increase the outgoing electron's energy; thus, the inelastic mean free path is larger and so is the probing depth. Therefore, we can measure different ratios of oxide/black phosphorus by changing the photon's energy. We illustrate this by comparing the probing depth of $h\nu_1$ and $h\nu_2$, where $h\nu_2 > h\nu_1$.

peaks related to the oxide and pristine black phosphorus. We followed the equation of Tanuma et al [67] to calculate the IMFP on black phosphorus for each kinetic energy. Finally we plot the area ratio as function of the inelastic mean free path, which can be adjusted using the equation 2.3 derived at Chapter 2 and Appendix D to determine the oxide thickness τ (Figure 3.6). The constant multiplicative term $\frac{I_{OX}}{I_{BP}}$ renamed as α was also fitted. From this dataset, we obtained a

value of 1.16 ± 0.08 nm for the oxide thickness.

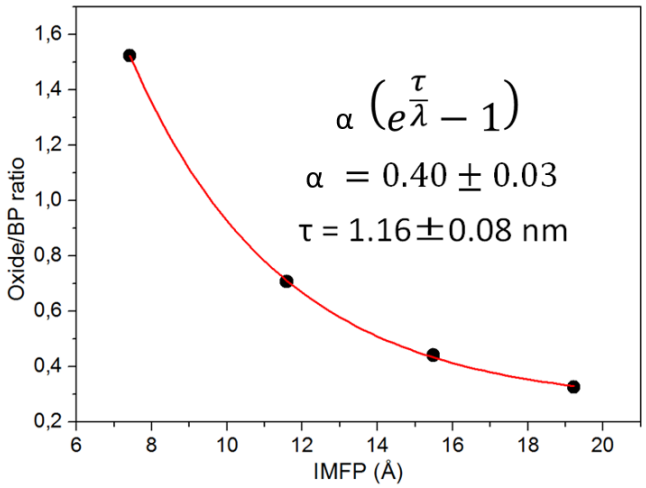

Figure 3.6: Depth profile graph of oxide/BP ratio by IMFP. Red curve is a fitted exponential curve to the points.

However, a comparative analysis with spectra measured at variable energies for different experiments, revealed that this thickness might be underestimated, since the depth profile was measured for an oxide that had not reached saturation yet. We did not followed this experiment kinetics and thus erroneously stopped the experiment before the oxidation had come to an end. In this particular experiment the ratio of the areas of the oxide and pristine peaks in the P_{2p} region for an incident photon energy of 330 eV and 730 eV were 1.5:1 and 0.44:1, respectively. Meanwhile, for O_2 exposure experiments in which the oxide reaches saturation (no further increase of the peak areas) these ratios are 2.05:1 and 0.6:1 respectively.

To circumvent this problem we had to extend our analysis to incorporate datasets for which the P_{2p} spectra were measured only at two photon energies, but under conditions where the oxide were definitely fully grown, like the red dots in Figure 3.7. These points alone are insufficient to define the exponential function, leading to huge uncertainties in the thickness. However, we can fit both datasets in conjunction using the same α, since this parameter is related to the intrinsic values of the signal intensity of both the oxide and black phosphorus and should have the same value independently of the oxide thickness (see Appendix C for more details). Hence, we obtain the fit by the green curve in Figure3.7, which results in a thickness of 1.35 ± 0.08 nm for the kinetically limited oxide layer.

Considering that the thickness for a phosphorus oxide layer has been calculated by DFT to be around 0.46 nm [36], we can assume to have something close to 3 layers of phosphorene oxide. This ultrathin native oxide, although not a monolayer as speculated by others, can still offer tremendous opportunities for technology and future research. Edmonds *et al.* were the first to perform a depth profile of an oxide grown atop black phosphorus [39]. Their experiment consisted of exposing a black phosphorus flake to atmospheric conditions of gases and light for a period of 28 days. They observed that the XPS spectra taken at day 2 was

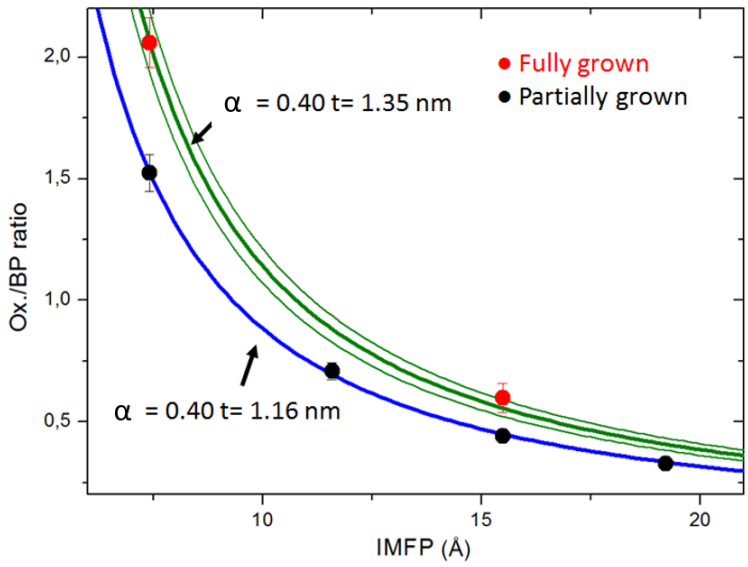

Figure 3.7: Depth profile graph, where we have the partially grown oxide data (black dots) and the completely grown oxide data (red dots). The blue curve is the fitting for the partially grown oxide. The green lines are the fittings of the fully grown oxide with α parameter fixed, the middle line is for $\alpha = 0.40$, whereas the superior and inferior green curves are the fitting for $\alpha \pm 0.03$, accounting for the error of the parameter.

very similar to the one taken at day 28. Assuming that the oxide ceased to grow, they measured spectra at different photon energies as indicated in Figure 3.8

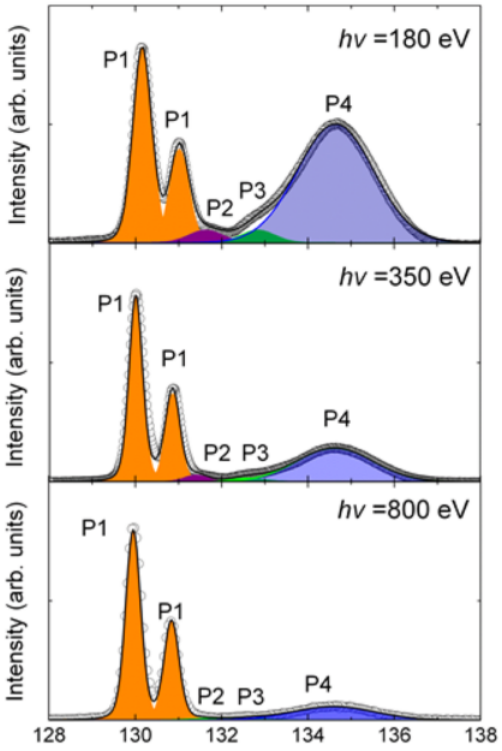

Figure 3.8: Depth profile of a black phosphorus crystal after 2 days in ambient air. Adapted from reference [39].

Using the ratio between the areas of the peaks labeled as P4 a P1 (or Ox./BP ratio) for different energies they determined a thickness of 0.40 ± 0.03 nm. This is a very contrasting result compared to our thickness of 1.35 ± 0.8nm. Unfortunately Edmonds *et al.* did not publish their respective area ratios, but one can safely compare their P_{2p} spectrum at 350 eV photon energy (Figure 3.8) to our spectrum at 330 eV (Figure 3.4). It is clear that for similar photon energies, for instance 330 and 350 eV , the intensity of the oxide features relative to the pristine phosphorus are considerably higher in our work than reported by Edmonds et al. The small kinetic energy difference of 20 eV cannot account for such enhancement of the oxide features in our case. In fact, our spectrum measured at 330 eV resembles more the spectrum of Edmonds measured at 180 eV. This clearly indicates that the oxide grown on the surface of black phosphorus in our experiments is considerably thicker than the one reported by Edmonds et al.

These differences in XPS spectra and oxide thickness can be explained by two mutual reasons. At first, one can think that Edmonds' oxide was not yet fully grown, since it did not presented the expected ratios. Secondly, Edmonds' experiment was performed in a non-controlled environment while our experiment was performed on a controlled oxygen atmosphere with controlled incidence of light. Moreover, perhaps these oxides are not derived from the same oxidation reaction or are not the same, thus presenting different results for the oxide thickness.

3.3 Oxidation Kinetics

We are now interested in quantifying the kinetics of the oxidation reaction evidenced by the time evolution of the spectra in Figure 3.1-c,d and Figure 3.2. In this section, we construct a reaction model based on observations from our experiments and the literature. Firstly, control experiments in which we exposed black phosphorus to oxygen in the dark (no visible light or X-rays) for many hours shows no evolution of the XPS spectra, indicating that the oxidation process is photoactivated, in agreement with other reports from the literature [37, 42]. Secondly, our results indicate that oxygen reacts not only with the surface of black phosphorus, but also totally consumes adventitious carbon contamination, which are usually difficult to remove from the surface. Hence, in our first reaction step, we assume that oxygen at the surface of black phosphorus is photoactivated generating a reactive oxygen species (O^*) with a reaction rate constant k_1.

$$BP + O_2 \xrightarrow{k_1, h\nu} BP + O^*$$

After formed, this reactive oxygen species (ROS) will diffuse on the surface and react readily with any atom it encounters on their way. This ROS will sometimes react with the phosphorus atoms at the surface of the black phosphorus at a reaction with a rate constant k_2^P

following multiple oxidation steps towards the final phosphorene oxide (PO):

$$O^* + BP \xrightarrow{k_2^P} PO$$

If the ROS, on the other hand, finds carbons species on the surface, it will react with them with a reaction rate constant k_2^C at consecutive oxidation steps until carbon dioxide is formed and subsequently leaves the surface of the black phosphorus:

$$O^* + C \xrightarrow{k_2^C} CO_{2(gas)}$$

We summarize the main features of our reaction model in figure 3.9. In this model, the nature of the reactive oxygen species is not specified, it could be either a charged oxygen molecule, oxygen radical, oxygen peroxide, superoxide or singlet oxygen. Regardless of its nature, we assume that once the oxygen molecule has been activated, it will readily react with whichever it comes in contact. Recent experiments reported by Hui et al. [27] suggest that singlet oxygen might be formed on the surface of black phosphorus upon visible light illumination, although the formation mechanism is not specified.

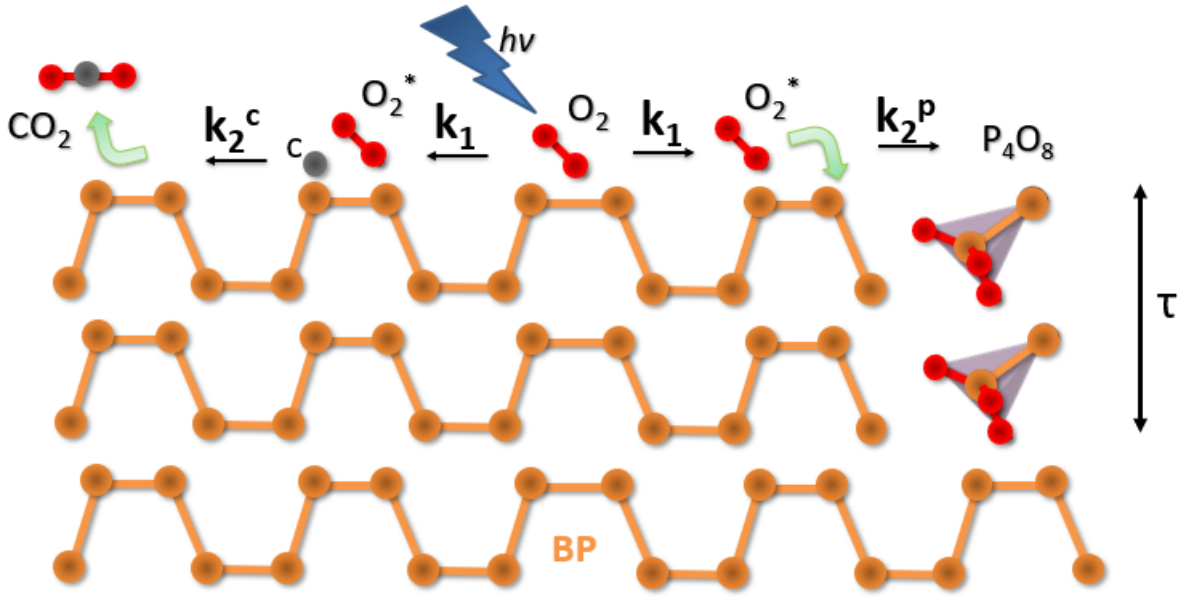

Figure 3.9: Kinetic model where we have an oxygen gas molecule being photoactived atop black phosphorus at a rate k_1, afterwards this reactive oxygen species (ROS) will react either with the black phosphorus or the adsorbed carbon at rates k_2^p and k_2^c, respectively. The ROS will react with black phosphorus forming phosphorene oxide (illustrated here by the oxide P_4O_8) with a layer of thickness τ.

In our experiments, for which the photochemistry is driven by X-rays, the formation

mechanism of the reactive oxygen species is also still unknown. We speculate an indirect photocatalytic process in which the X-ray are absorbed by the phosphorus creating holes mostly at the core-levels, which inevitably relax in a cascade of Auger and fluorescence decays, leading to an abundance of shallow holes at valence levels. This population of holes in the valence band (or electrons in the conduction band), named in the photochemistry literature as hot carriers, are considered to be related to the photocatalytic molecular oxygen activation towards superoxide. On the other hand, the production of singlet oxygen is more reasonable to undergo by energy transfer process that involves spin-triplet excitons to overcome the spin-flip restrictions [27].

Using this reaction model with the assumption of consecutive first order reactions (rates linearly dependent on concentration), we construct a system of differential equations that can be solved to determine the concentration of each reaction product as function of time. Further details including the differential equations and approximations are given in Appendix C. Equation 3.1 is the solution for the concentration of phosphorene oxide as function of time.

$$[PO](t) = [BP]_0 \left(1 + \frac{k_1 e^{-k_2^p(t)} - k_2^p e^{-k_1 t}}{k_2^p - k_1}\right) \tag{3.1}$$

Note that the phosphorene oxide concentration is described by a two-phase exponential growth curve dependent on both rate constants k_1 and k_2^p. But, a visual inspection of Figure 3.10-b that shows the O_{1s} area as function of time tells that the curve seems prominently related to a single exponential. In fact, attempts to fit a double exponential curve to the experimental data results in one of the rate constants much smaller than the other. Fortunately, one can address this issue analytically with a simple approximation, assuming that $k_1 << k_2^p$ in Equation 3.1, which results in Equation 3.2 with a single exponential function dependent on k_1 only.

$$[PO](t) = [BP]_0 \left(1 - e^{-k_1 t}\right) \tag{3.2}$$

This approximation can be rationalized by considering two factors: 1) The X-ray induced photocatalytic activation of molecular oxygen is an inefficient and slow process. 2) After formed, the ROS reacts very fast at the surface. Therefore, it is reasonable to assume that the reaction rate constant k_2^p is much higher than k_1.

Following similar arguments detailed in appendix C, we can derive an expression for the concentration of surface carbon as function of time given by Equation 3.3.

$$C(t) = e^{-k_1 t} \tag{3.3}$$

Finally, we can use the equations 3.2 and 3.3 to fit the experimentally measured reaction kinetics in Figure 3.10-a,b and determine values for the rate constants. Remarkably, we achieved extremely similar values for the rate k_1 as 3.1 ± 0.01 and $3.2 \pm 0.01\ 10^{-4} s^{-1}$ by fitting the independent datasets related to the areas of the C_{1s} and O_{1s} peaks, respectively. This

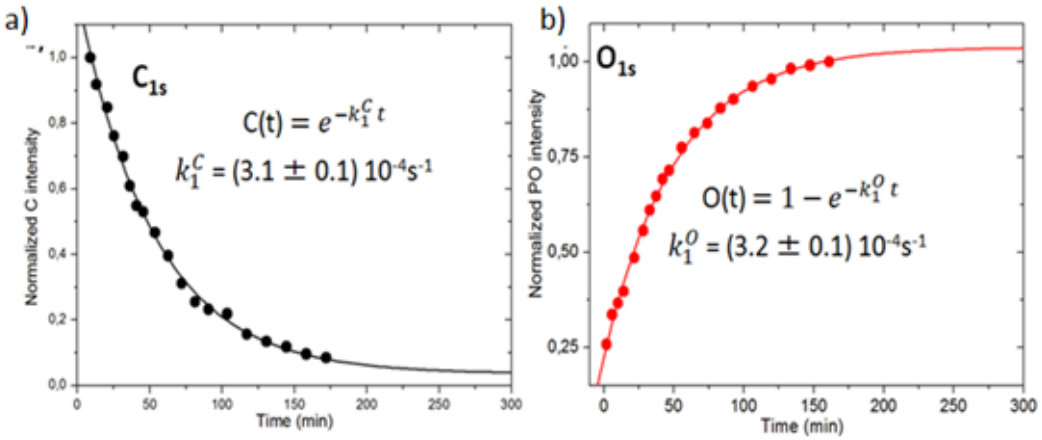

Figure 3.10: a) Carbon area intensity by time. b) Oxide area intensity by time, along with each curve's exponential fit. We can see that both these curves have the same reaction rate.

indicates that our model and approximations can describe well the observed reaction kinetics.

We conclude that in our experimental conditions the molecular oxygen activation is the rate limiting step of the reaction, which results in the slow reaction kinetics. Hence our kinetic data cannot be used to infer information about the reaction of oxygen with phosphorus or the origin of the limited oxide growth. However we can speculate few possibilities based on oxidation mechanisms proposed for other systems.

The Cabrera-Mott model is a very well established interpretation of oxide growth and can be applied, although not strictly, for thin oxide films growing atop metals and semiconductors [68, 69], as in the case of our 1.35 nm thick oxide. Summarizing, the model basis itself on the premise that electrons can freely traverse from the oxide/metal interface towards the surface, where they ionize oxygen atoms. Whilst activating oxygens, these electrons also produce a field in the oxide layer. This field is then responsible for the shift of the oxide's fermi-level and the ionic transport throughout the thin film. This transport could be either from metal atoms towards the surface, or oxygen atoms towards the interface.

In our case, since there is no oxidation in the dark, the drive of electrons towards the surface is not spontaneous, even when the oxide layer is close to null. Thus, only when photons are present that the electrons' motions is set and the Mott potential is generated. Through our measurements it is not possible to identify if the ionic transport is given by the oxygen atoms diffusing towards the interface or the phosphorus atoms towards the surface. Much like Aluminum oxidation, the oxidation of black phosphorus is limited. This limitation could be derived from the inability of the ionic carrier to diffuse through the oxide layer after a certain thickness is achieved. Electronic effects could also pose limitations to the growth. As will be discussed in section 3.5, we have spectroscopic evidences that suggest charge transfer between the oxide and black phosphorus underneath. These effects could be the limiting factor of the oxidation.

One conclusion we can draw from our measurements is that the electron transport

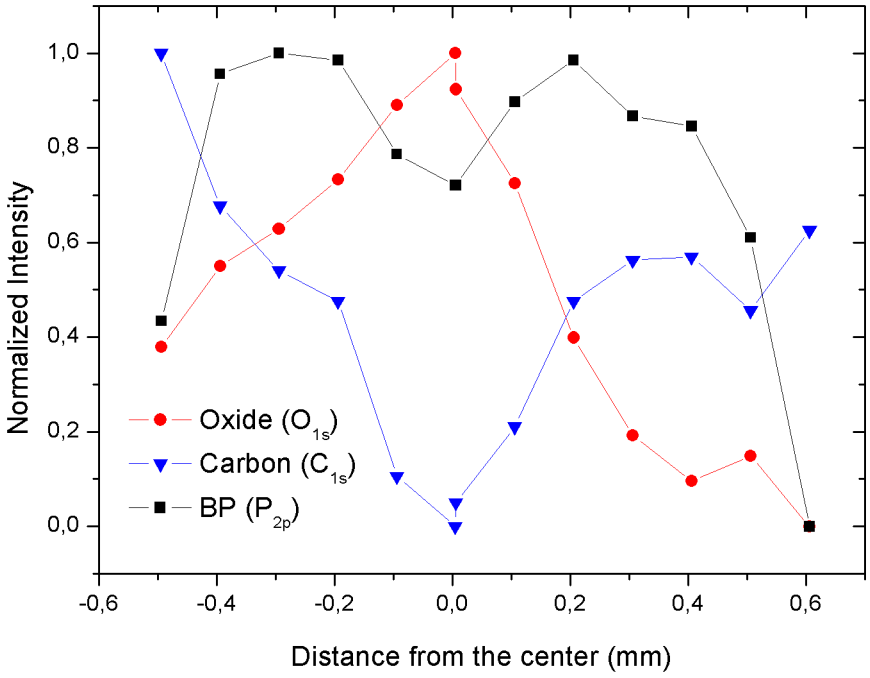

Figure 3.11: XPS line scan in UHV of the black phosphorus flake after oxidation. Position 0 is the beam position during oxidation. The asymmetry between the right and left scans can be attributed to the uncertainty in the movement of the beam.

towards the surface is not the limiting factor. Figure 3.11 shows the integrated areas for peaks related to Oxygen, Phosphorus and Carbon as function of the lateral distance from the point where the photo-oxidation took place. One can see that as one move away from the center of irradiation, we have the attenuation of oxide signal and the increase in carbon signal. The pristine black phosphorus signals presents a parabola shape. This is due to the fact that the black phosphorus' signal is attenuated at the center by the oxide layer and in the far regions by the carbon contaminants. The beam size is 0.1x0.1 mm full width at half maximum, therefore the black phosphorus' surface that was illuminated by the beam during oxidation extends 0.05 mm towards each side. The oxide signal halves somewhere in between 0.2 to 0.4 mm away from the center. That's at least 4 times further away from the center of irradiation than the beam. Which implies that the ROS migrated away from the center after this region ceased to oxidize and reacted with the nearby surface lying in the dark.

3.4 Phosphorene Oxide Atomic Structure

One of the main objectives of this work is to study the atomic structure of the phosphorene oxide grown on the surface of black phosphorus. Therefore, we exposed a crystal to 13 mbar O_2 atmosphere and 730 eV photon beam for approximately 3 hours. Afterwards we

measured high resolution XPS spectra of the P_{2p} and O_{1s} regions. These high resolution spectra are shown at Figure 3.12. The P_{2p} region was measured with a photon energy of 330 eV, whilst the O_{1s} was measured with a 730 eV photon beam, in order to have both regions with the same kinetic energy.

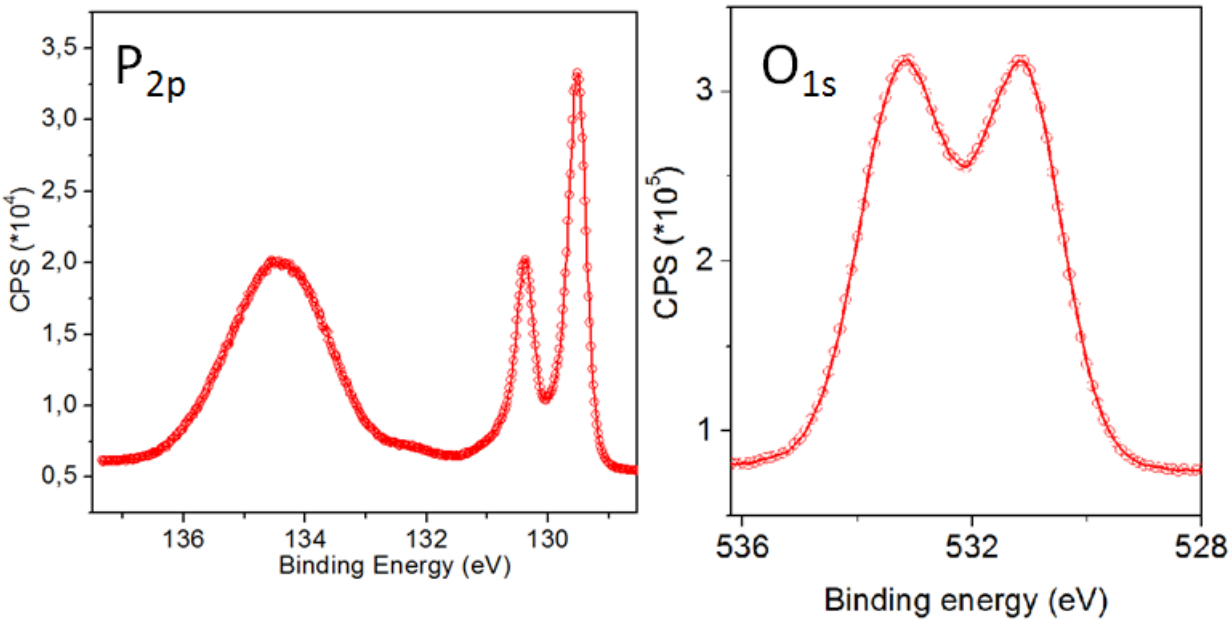

Figure 3.12: High resolution XPS spectra of the P_{2p} and O_{1s} regions of an oxidized black phosphorus flake. Measured with 330 eV and 730 eV, respectively.

In the literature, it is known that phosphorus oxides presents two distinct oxygen species [36]. One of these species is the *dangling* oxygen, where the oxygen atom solely bond to one phosphorus atom (P=O). Secondly, we have the *bridge* oxygen species, where an oxygen atom is bonded to two phosphorus atoms, bridging them (P-O-P). These oxide motifs are represented in Figure 3.13. By taking a closer look at the O_{1s} spectrum at Figure 3.12, one can clearly see that the overall feature is the sum of two distinct peaks. Each of these peaks belongs to either one of these species, since the 1s orbital of oxygen does not present spin-orbit coupling.

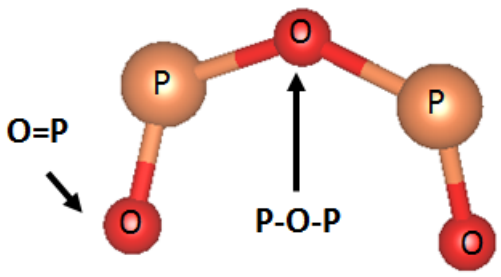

Figure 3.13: Oxygen and phosphorus atoms of a generic phosphorus oxide. Highlighting the bridge (P-O-P) and dangling oxygen (P=O).

Using the method described at Appendix A, we fitted 2 Gaussian-Lorentzian peaks to the O_{1s} spectrum (Figure 3.14). The two peaks appears at binding energies of 531.04 eV and 533.09 eV. Assisted by DFT calculations performed by our collaborators, we assign the peak with higher binding energy to the bridge oxygen species and the lower binding energy to the dangling oxygen species. This assignment agrees other reports on the literature for bulk phosphorus oxides [50]. The difference of binding energies between these peaks is $\Delta B.E. = 2.05$ eV. This is also a useful measurement to compare to DFT calculations. It is worth mentioning, that fitted areas of the bridge and the dangling oxygen peaks are nearly the same (ratio of 1.002), indicating that we have an equal number of both oxygen species in the oxide structure.

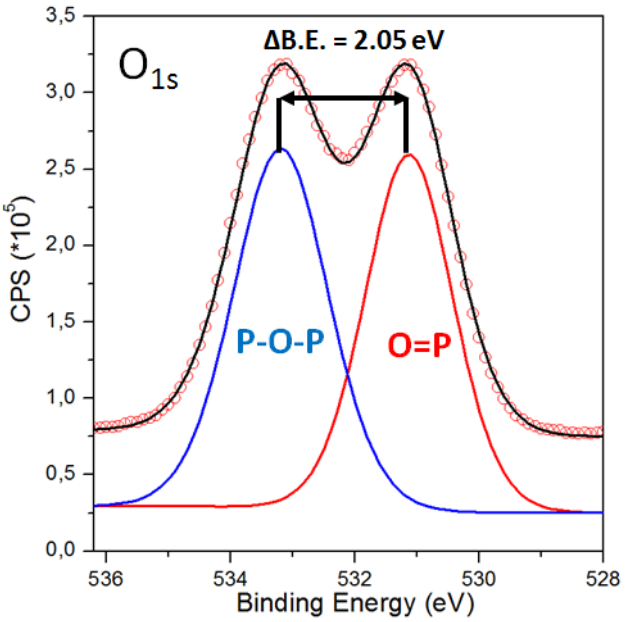

Figure 3.14: O_{1s} spectrum. Red dots are the measured XPS signal. Black line is the adjusted peaks sum envelope. Fitted peaks for the bridge oxygen (blue line) and dangling oxygen (red line). Measured with 730 eV.

At the P_{2p} spectral region, we fitted 4 sets of components, as shown in the Figure 3.15, each of them with their respective spin-orbit doublet with a fixed intensity ratio of 2:1. The first set of components at 134.16 eV is assigned to the phosphorene oxide (PO), based on the literature and DFT calculations. Around 132 eV, there is small set of peaks that is related to a contamination that we will address later in section 3.6. The last 2 set of peaks are assigned to the pristine black phosphorus at 129.74 eV and the phosphorus atoms at the interface with the oxide at 129.51 eV. The core level shift and this difference of binding energy between top and inner layers of pristine black phosphorus will be discussed in the next section.

We calculated the oxide stoichiometry by dividing the area beneath the curves of the oxygen species in the O_{1s} spectrum by the area of the P_{2p} phosphorene oxide feature and correcting this ratio by factors to account for the analyzer transmission, orbital asymmetry, photon flux and effective photo-ionization cross-section differences. The procedure is detailed

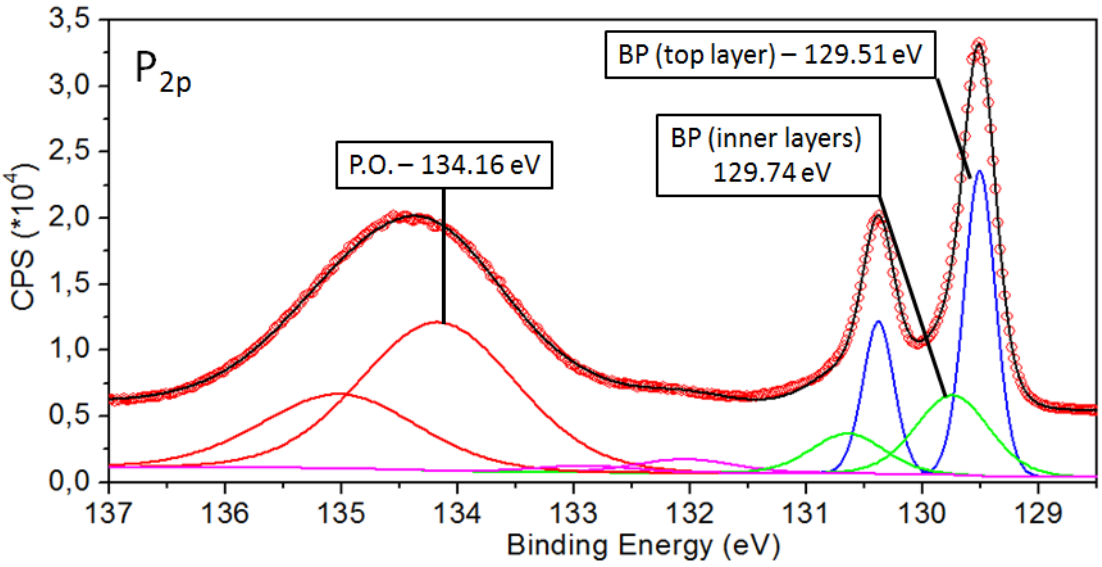

Figure 3.15: P_{2p} spectrum. Red dots are the measured XPS signal. Black line is the adjusted peaks sum envelope. Fitted peaks for the pristine black phosphorus (blue and green line) and phosphorene oxide (red line). Measured with 330 eV.

in Appendix B. The achieved stoichiometry of oxygen and phosphorus atoms in the oxide is 1.9 ± 0.2:1, which is fairly close to 2:1.

The phosphorus pentoxide (P_2O_5) is widely regarded in the literature as the most probable oxide formed on the surface of black phosphorus, since it is the most thermodynamically stable phosphorus oxide in the bulk form [36, 39, 49, 50]. In fact, a planar structure of P_2O_5 has already been proposed by some authors [36, 49] to be growing atop black phosphorus. Phosphorus pentoxide's stoichiometry is 5:2 (or 2.5:1), and the ratio between bridge and dangling oxygens is 3:2 (or 1.5:1). In contrast, we determined a stoichometry of 2:1 and ratio of oxygen species 1:1, indicating that P_2O_5 is not the oxide growing at the surface black phosphorus in our experimental conditions.

Using the quantitative data of our experiments, we propose that the surface oxide growing across the surface is the diphosphorus tetraoxide (P_4O_8) in planar or tetragonal form. Its structure is very similar to the P_2O_5 proposed in the literature (Figure 3.16). The difference lies that in our proposed structure one phosphorus-phosphorus bond remains intact, the interstitial one (Figure 1.2). This reduce the number of bridge oxygens in the structure. This structure has a 2:1 stoichiometry and 1:1 oxygen species ratio, matching our experimental data. The DFT calculations of our collaborators indicated that the P_4O_8 structure shown Figure 3.17 is thermodynamically stable.

An interesting test is to compare the measured binding energies with DFT calculations for both P_4O_8 and P_2O_5 structures. Since absolute binding energy are prone to uncertainties in DFT calculations, we use only energy differences for comparisons. The difference between the binding energies of the oxygen species in the O_{1s} spectral region (ΔB.E.(bridge-dangling)) and between the phosphorene oxide and pristine black phosphorus in the P_{2p} spectral

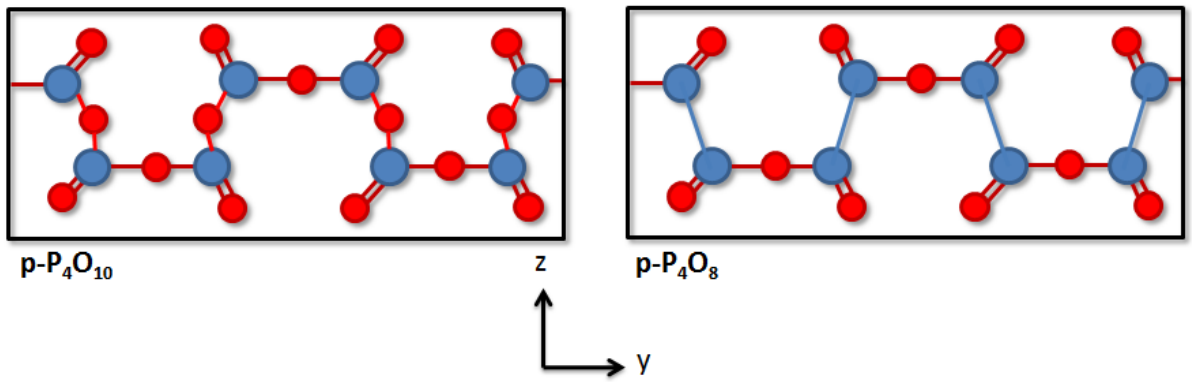

Figure 3.16: Comparison between the planar P_2O_5 and P_4O_8 structures. Blue circles represents phosphorus atoms and red circles represents oxygen atoms.

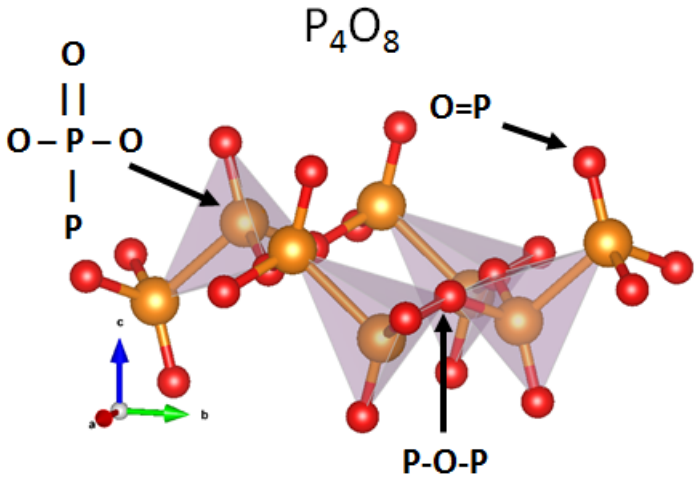

Figure 3.17: DFT calculated P_4O_8 structure, with highlighted phosphorus and oxygen species.

region (ΔB.E.(PO-BP)) experimentally measured and calculated are shown in Table 3.1.

Table 3.1: Comparison between measured and DFT calculated (P_4O_8 and P_2O_5) binding energy differences for the O_{1s} and P_{2p} spectral regions.

ΔBE	P_2O_5	P_4O_8	Experiment
O_{1s}(bridge-Dangling)	2.3	2.0	2.05
P_{2p}(PO-BP)	5.5	3.6	4.42

The values in Table 3.1 suggest that the P_4O_8 structure shows a better agreement with the experimental observations that the P_2O_5. This is more noticeable when looking at the binding energy difference between the oxygen species, for which the P_4O_8 differs from the measurement by just 0.05 eV. These binding energies data and the stoichiometry favors the hypothesis that the phosphorene oxide is, in fact, a diphosphorus tetraoxide.

Contrary to our observations, Edmonds *et al.* concluded the formation of a P_2O_5 structure on their experiments [39] based on literature calculations of absolute binding energies

[70, 71] for the P_{2p} region only. However, absolute energy calculations are not very trustworthy, due to large uncertainties in DFT calculations. Moreover, they neither measured the O_{1s} spectral region to compare the binding energies or to account for the stoichiometry, basing their entire hypothesis on a single measurement of the binding energy of the oxide peak.

3.5 Electronic Structure of the Heterostructure

By following the evolution of the spectra during our oxidation experiments, we observed that the peaks were shifting their binding energies. All the peaks present at the P_{2p} (Figure 3.18) and O_{1s} (Figure 3.19) spectral regions showed the same behavior. The oxide related peaks on both regions appear to shift towards higher binding energies, while the peaks related to pristine black phosphorus shifts towards lower binding energies. Moreover, these shifts cannot be attributed to sample charging, since they do not occur all in the same direction towards higher binding energies.

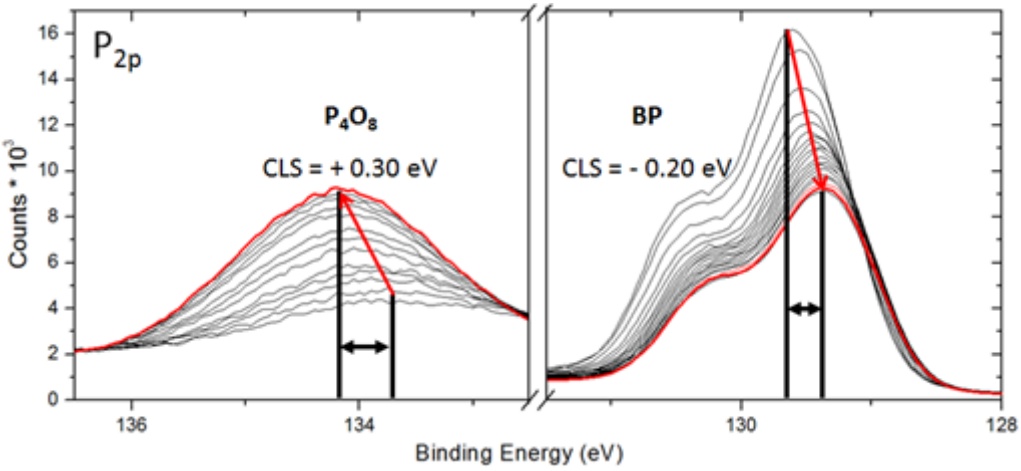

Figure 3.18: P_{2p} spectral region showing the peaks of the P_4O_8 and pristine black phosphorus (BP). Red line is the last measurement. Core-level shifts of +0.30 eV e -0.20 eV are evidenced.

If we compare the first spectrum with the last one, we can clearly observe a core-level shift (CLS) of approximately +0.30 eV for the phosphorene oxide P_{2p} peak and -0.20 eV for the pristine black phosphorus. Likewise, both oxygen features suffer a core-level shift of +0.20 eV. The origin of such core-level shifts can be traced to several different factors such as band bending, surface states and interface dipoles [72]. Currently, considering our heterostructure model, our interpretation of these shifts is the charge transfer between the oxide layer and the phosphorene layers underneath, forming a dipole in the interface region as illustrated by Figure 3.20.

Core-level shifts are also present in the P_{2p} spectra from the depth profile experiment discussed in section 3.2. To see how the CLS change as function of the probed depth, we measured the binding energy difference between the pristine black phosphorus peak after

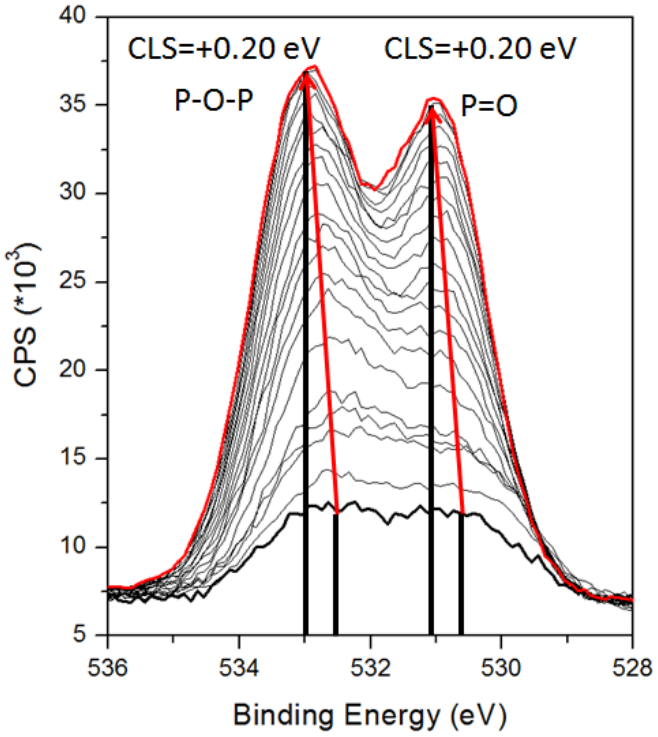

Figure 3.19: O_{1s} spectral region showing the peaks of the P_4O_8 and pristine black phosphorus (BP). Red line is the last measurement. Core-level shifts of +0.30 eV e -0.20 eV are evidenced.

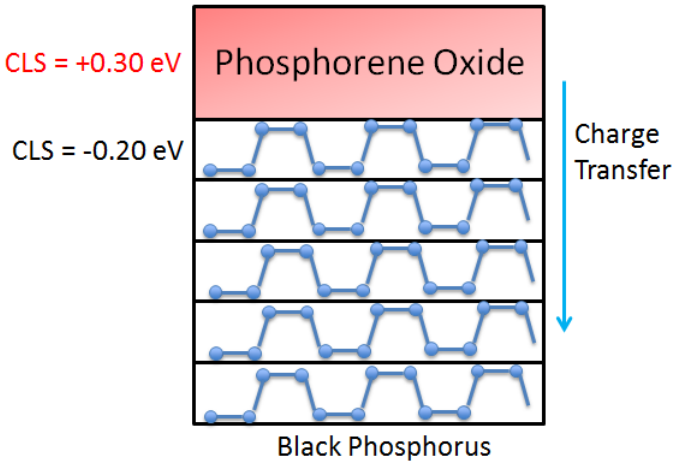

Figure 3.20: Charge transfer scheme from the phosphorene oxide layer to the pristine black phosphorus underneath.

oxidation for different probed depths (IMFP) and the peak of the unoxidized flake. Figure 3.21 shows that the core-level shift decrease exponentially with depth, which further corroborates our charge transfer hypothesis. Moreover, since the real binding energy difference is then smaller than the one perceived on experiments probing lower depths, the experimental value for this difference gets even closer to the calculated P_4O_8 values.

To learn more about the electronic structure of the BP-oxide heterostructure, it is

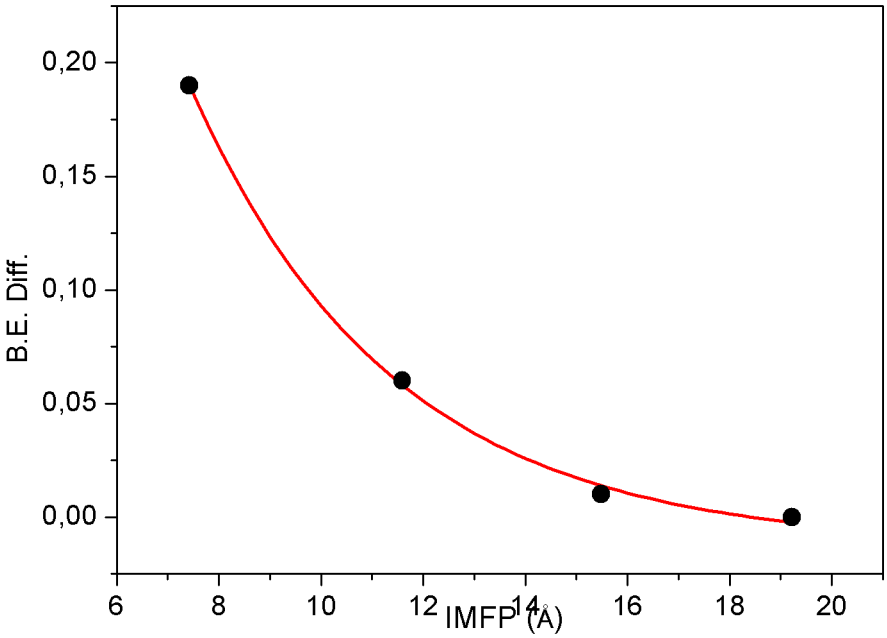

Figure 3.21: Binding energy difference of the pristine black phosphorus peak after oxidation and the unoxidized peak as a function of the inelastic mean free path of the outgoing electrons.

worth to look at the valence levels. Figure 3.23-a shows valence band before (black) and after (red) the oxidation of the black phosphorus with a 330 eV photon energy under O_2 atmosphere. We can observe small shift of the the valence band maximum (VBM), which is magnified in Figure 3.23-b for better visualization. The VBM before the oxidation was positioned at 0.43 ± 0.01 eV, whereas after the oxidation the VBM suffered a -0.14 eV shift towards the Fermi level, reaching a value of 0.29 ± 0.03 eV. This negative shift of the valence band agrees with the core-level shift of the pristine black phosphorus towards lower binding energies. This is another corroboration for the charge transfer hypothesis.

The valence region can also be used to test the structural models. The density of states (DOS) of the oxide structures P_4O_8 and P_2O_5 were calculated by DFT. Figure 3.23 shows a comparison of these calculations with the experimental measurement of the valence band of the heterostructure after oxidation. Note that to compare with the experimental data we did a linear combination of the DOS calculated for the oxide structure and pristine BP, since the XPS probes all the layers comprising the heterostructure. The calculated DOS for both oxide structures compares well with the most prominent peaks of the experimental measurement in the region from 0 to 10 eV. But we should emphasize that there is a better agreement between the P_4O_8 calculations with the experimental data for the region further away from the Fermi level, between 10 and 15 eV, in comparison to P_2O_5. Although the energy resolution of the valence levels is not enough to clearly distinguish between oxide structures, it can be used as an

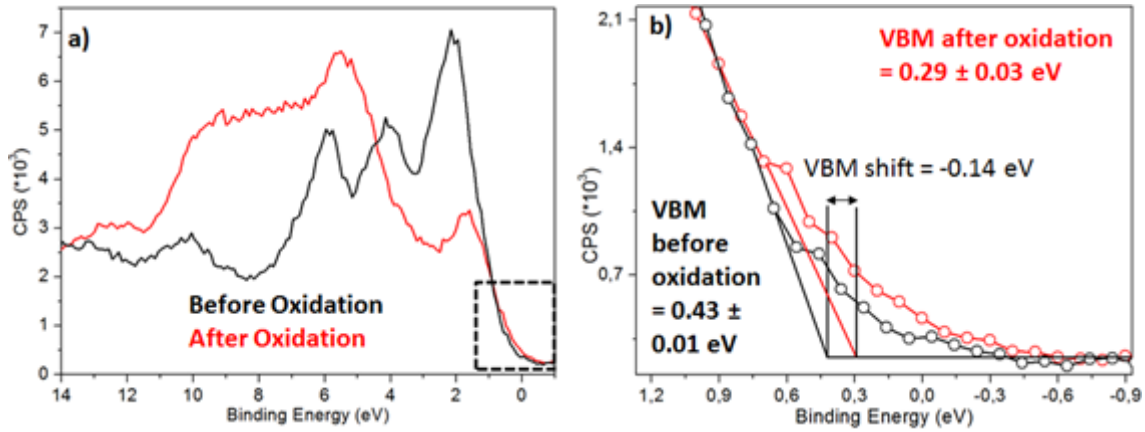

Figure 3.22: a) Valence band before (black line) and after (red line) of oxidation. b) Magnification of the marked region in (a). Where is measured the valence band maximum (VBM) before (black line) and after (red line) of oxidation. VBM shift is of -0.14 eV.

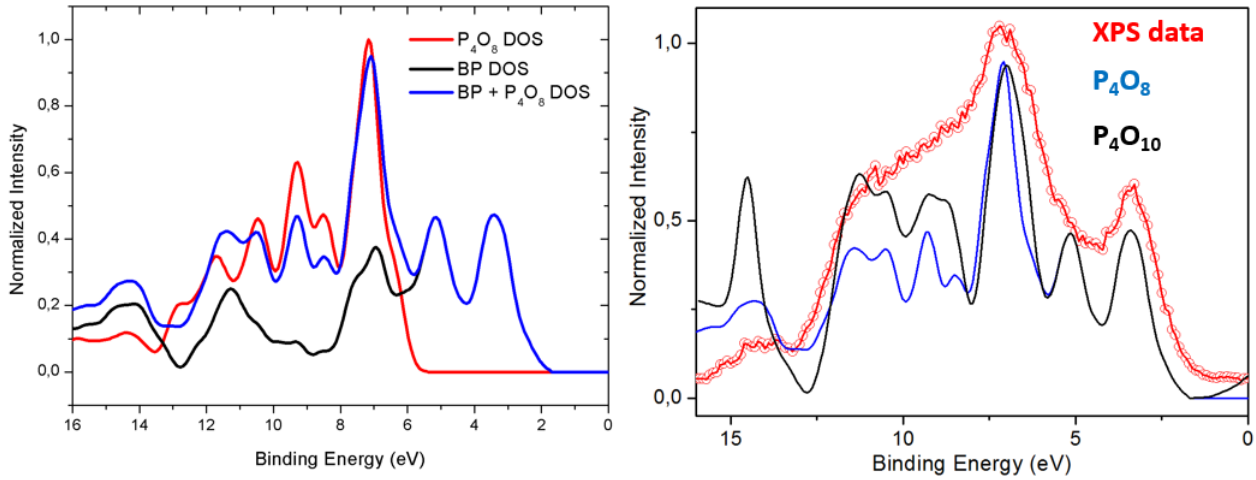

Figure 3.23: a) Density of states (DOS) calculations of the pristine black phosphorus (BP) and for the P_4O_8. Along with the weighted sum of both. b) Valence band comparison of the measured oxidized valence band (red dots) with the DFT calculations of the density of state for the P_4O_8 structure (blue line) and the P_2O_5 (black line). The density of states of the oxides are in convolution with the density of states calculated for the pristine black phosphorus.

additional evidence in favor of the P_4O_8 in agreement with our core-level data.

3.6 Nitrogen Interaction

During an experiment where we exposed a freshly cleaved black phosphorus flake to a 1 mbar O_2 + 1.3 mbar H_2O atmosphere under a 730 eV photon beam, we perceived that a feature appeared on our XPS spectra at about 400 eV (Figure 3.24). Which is the N_{1s} spectral region. Therefore, we speculated we had a leak of nitrogen gas into the experimental chamber. The features appearing at 400 eV are in fact, bonded nitrogen atoms. Which is remarkable due to nitrogen gas' known resilience to react.

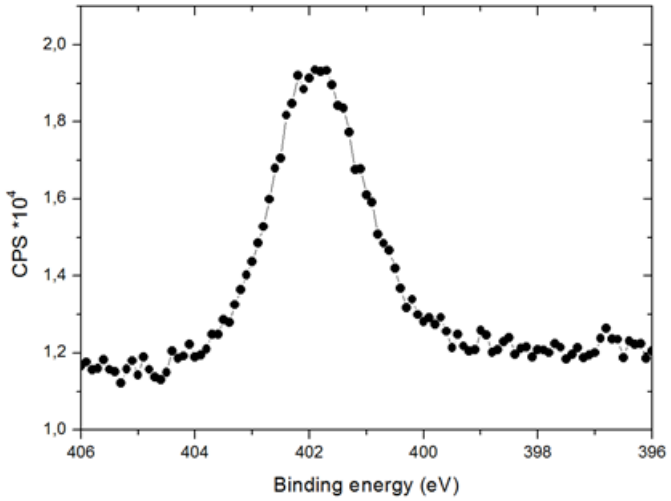

Figure 3.24: N_{1s} spectral region measured with 600 eV.

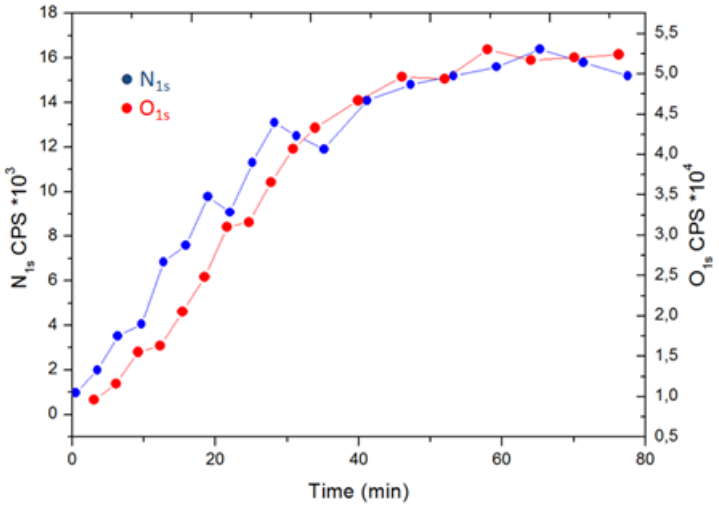

Figure 3.25: Growth of the features on the N_{1s} spectral region and at the O_{1s} region (oxide) as a function of time for the 1 mbar O_2 + 1.3 mbar H_2O atmosphere experiment. Both measured with 730 eV photon beam.

Aware of the nitrogen leak, we also followed the N_{1s} spectral region during the experiment. The areas of the features present at N_{1s} were obtained and plotted as a function of time at Figure 3.25 alongside the area of the features of the O_{1s} spectral region. Both growth curves are extremely similar, which suggest the same reaction rate and path. It is possible that the reactive oxygen species is also reacting with the residual nitrogen molecules, forming nitrogen atoms that readily react with the black phosphorus surface.

Using the same method as used in Appendix B, we calculated how much intensity would a P_xN_y peak yields in the P_{2p} spectral region, in comparison to the intensity we get at the N_{1s}. For our surprise, it would be almost exactly the same as a non-attributed small peak between the black phosphorus peak and the oxide peak in the P_{2p} spectral region, as shown in Figure 3.26.

Therefore, we finally managed to assign the small peak at around 132.05 eV. Fur-

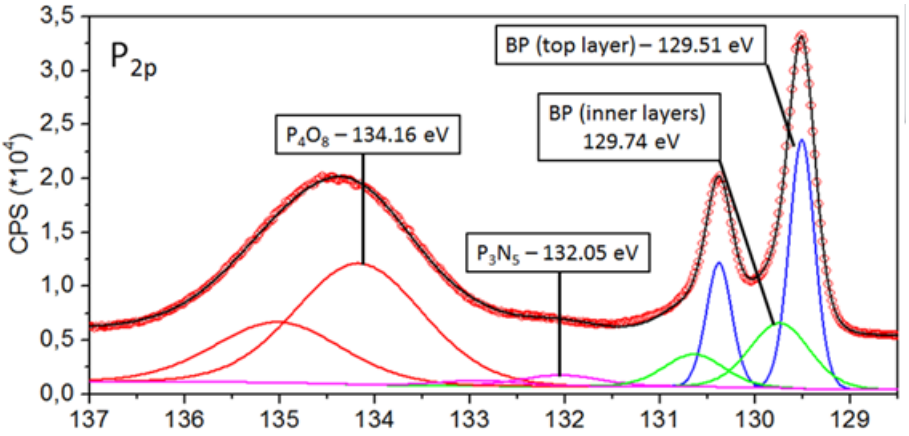

Figure 3.26: High resolution spectrum of the P_{2p} spectral region, with the BP peaks of both top and inner layers, the P_4O_8 peak and the notorious P_3N_5 peak.

thermore, we discovered that the ratio between the nitrogen and phosphorus in our measurements for this P_xN_y compound was approximately 5:3, relating to the compound P_3N_5, the most common phosphorous nitride. We need to confirm this assignment by DFT calculations.

Chapter 4

Conclusions and perspectives

4.1 Conclusions

4.1.1 Gas interactions

During our AP-XPS experiments of black phosphorus' oxidation under a controlled atmosphere we reached the conclusion that water, by itself, does not oxidize phosphorene. This result agrees with the work of Wang *et al.*[53] and calculations of Zhou *et al.*[49]. On the other hand, we could observe the formation of a layer of phosphorene oxide when black phosphorus was exposed solely to a dry oxygen atmosphere, in contrast to Luo *et al.*[50] that only managed to grow the oxide in a wet oxygen atmosphere. Following the oxidation kinetics in situ, allowed us to clearly observe the growth rate saturation, contrary to Edmonds *et al.*[39] and Luo *et al.*[50] who could not tell if the oxide was really completely grown. Therefore, we here present data confirming that the oxide growth is limited suggesting the formation of a passivation layer that prevents further oxidation. We also noticed that nitrogen also reacted with the surface of black phosphorus, forming a phosphorus nitride. This is the first time a research group has observed the reaction of nitrogen with the surface of black phosphorus. This could lead to new research regarding the chemistry of black phosphorus.

4.1.2 Oxide thickness

Once understood that the oxide grew to a certain depth and ceased growth, we used depth dependent AP-XPS measurements to unravel the oxide thickness. Using simple structural model to analyze P2p spectra measured at different photon energies for samples exposed to oxygen at diferent times, we managed to estimate the oxide thickness to be 1.35 nm. Comparing to the calculations of a monolayer of phosphorus oxide of Ziletti *et al.*[36] of 0.46 nm, we estimate to have around 3 monolayers of oxide. Edmonds *et al.* [39] estimated an oxide layer of 0.40 nm to grow atop black phosphorus when exposed to ambient environment. However, they did not had the control of the oxide growth and they did not specify the sample quality, hence,

these measurements could've been performed on an incomplete oxide layer.

4.1.3 Atomic and electronic structure

We used AP-XPS measurements to underscore the stoichiometry of the oxide. With our oxygen/phosphorus and dangling/bridge oxygens ratios, assisted by DFT calculations, we proposed that the phosphorene oxide is a diphosphorus tetraoxide (P_4O_8). This is in contrast to works in the literature that the identify the oxide on the surface of BP as P_2O_5 [36, 49].

The phosphorene oxide and black phosphorus forms a heterostructure. Our measurements also showed core-level and valence band shifts of the oxide and phosphorene layers. Whereas, the oxide shifts are towards higher binding energies and the phosphorene towards lower binding energies. Since we have two different directions for the shift, we do not have a charge buildup. We believe we have a charge transfer from the oxide to the phosphorene forming a dipole at the interface. This charge transfer could be useful in the design of a BP-device.

4.1.4 Reaction kinetics

We followed the kinetics of the evolution of AP-XPS spectra of both oxygen, phosphorus, nitrogen and carbon regions. We modeled the oxidation reaction kinetics according to these measurements. We discovered that both oxide growth, nitride growth and carbon removal are all governed by the same global rate k_1. This rate is related to the photo-activation of the oxygen into a reactive oxygen specie. This is the limiting step, since it is present in all oxidation reactions and it's the slowest process of all.

4.2 Perspectives

We managed to achieve a lot of information regarding the interaction of black phosphorus with gases and its subsequent formation of the oxide. Along with the oxide atomic structure and electronic structure of the heterostructure. However a few questions remained unanswered. For a continuation of the project, we propose the following experiments and analysis:

- Kinetics AP-XPS measurements of the growth of the oxide under various oxygen pressures and different standalone laser light fluences to better understand if these play a role in the thickness of the oxide.

- Kinetics AP-XPS measurements of a clean black phosphorus flake to a wet oxygen atmosphere to evaluate the role of water in the oxidation process when it is started along with the oxidation by the oxygen. And the same measurements, but with a water atmosphere on an dry-oxygen oxidized flake, to evaluate the interaction of water with the passivated oxidized surface.

- Further development on the interaction of nitrogen with black phosphorus, now exposing BP to a controlled nitrogen+oxygen atmosphere.
- ARPES measurements of the oxidized surface to better understand the effects of the oxide in the electronic structure of the heterostructure.
- XANES measurements of the oxidized surface to compare with already calculated DFT data.

Bibliography

1. Housecroft, C. E. & Sharpe, A. G. *Inorganic Chemistry* ISBN: 0130399132 (2001).
2. Gusmao, R., Sofer, Z. & Pumera, M. Black Phosphorus Rediscovered: From Bulk to Monolayer. *Angewandte Chemie International Edition.* ISSN: 14337851 (2017).
3. Ling, X., Wang, H., Huang, S., Xia, F. & Dresselhaus, M. S. The Renaissance of Black Phosphorus. *Proceedings of the National Academy of Science* **112,** 4523–4530. ISSN: 0027-8424 (2015).
4. De Lima, L. H., Barreto, L., Landers, R. & de Siervo, A. Surface Structure Determination of Black Phosphorus Using Photoelectron Diffraction. *Physical Review B* **93,** 035448. ISSN: 2469-9950 (2015).
5. Tran, V., Soklaski, R., Liang, Y. & Yang, L. Layer-controlled band gap and anisotropic excitons in few-layer black phosphorus. *Physical Review B - Condensed Matter and Materials Physics* **89,** 1–6. ISSN: 1550235X (2014).
6. Rahman, M. Z., Kwong, C. W., Davey, K. & Qiao, S. Z. 2D phosphorene as a water splitting photocatalyst: fundamentals to applications. *Energy Environ. Sci.* **9,** 709–728. ISSN: 1754-5692 (2016).
7. Xia, F., Wang, H., Xiao, D., Dubey, M. & Ramasubramaniam, A. Two-dimensional material nanophotonics. *Nature Photonics* **8,** 899–907. ISSN: 17494893 (2014).
8. Rodin, A. S., Carvalho, A. & Castro Neto, A. H. Strain-induced gap modification in black phosphorus. *Physical Review Letters* **112,** 1–5. ISSN: 10797114 (2014).
9. Ostahie, B. & Aldea, A. Phosphorene confined systems in magnetic field, quantum transport, and supperradiance in the quasi-flat band, 1–24. ISSN: 2469-9950 (2015).
10. Li, L. *et al.* Black phosphorus field-effect transistors. *Nature nanotechnology* **9,** 372–7. ISSN: 1748-3395 (2014).
11. Xia, F., Wang, H. & Jia, Y. Rediscovering black phosphorus as an anisotropic layered material for optoelectronics and electronics. *Nature communications* **5,** 4458. ISSN: 2041-1723 (2014).

12. Liu, H. *et al.* Purdue e-Pubs Phosphorene: An Unexplored 2D Semiconductor with a High Hole Mobility Phosphorene: An Unexplored 2D Semiconductor with a High Hole Mobility. **8,** 4033–4041 (2014).

13. Koenig, S. P., Doganov, R. A., Schmidt, H., Castro Neto, A. H. & Özyilmaz, B. Electric field effect in ultrathin black phosphorus. *Applied Physics Letters* **104,** 103106. ISSN: 0003-6951 (2014).

14. Morita, A. Semiconducting black phosphorus. *Applied Physics A Solids and Surfaces* **39,** 227–242. ISSN: 07217250 (1986).

15. Qiao, J., Kong, X., Hu, Z.-X., Yang, F. & Ji, W. High-mobility transport anisotropy and linear dichroism in few-layer black phosphorus. *Nature communications* **5,** 4475. ISSN: 2041-1723 (2014).

16. Luo, Z. *et al.* Anisotropic in-plane thermal conductivity observed in few-layer black phosphorus. *Nature Communications* **6,** 1–32. ISSN: 2041-1723 (2015).

17. Wang, Y. *et al.* Remarkable anisotropic phonon response in uniaxially strained few-layer black phosphorus. *Nano Research* **8,** 1–10. ISSN: 19980000 (2015).

18. Carvalho, A. *et al.* Phosphorene: from theory to applications. *Nature Reviews Materials* **1,** 16061. ISSN: 2058-8437 (2016).

19. Mao, N. *et al.* Optical Anisotropy of Black Phosphorus in the Visible Regime. *Journal of the American Chemical Society* **138,** 300–305. ISSN: 0002-7863 (2015).

20. Wang, X. *et al.* Highly anisotropic and robust excitons in monolayer black phosphorus. *Nature Nanotechnology* **10,** 517–521. ISSN: 17483395 (2015).

21. Fei, R. *et al.* Enhanced Thermoelectric E ffi ciency via Orthogonal Electrical and Thermal Conductances in Phosphorene. *Nano Letters* **14,** 6393–6399 (2014).

22. Heremans, J. P., Dresselhaus, M. S., Bell, L. E. & Morelli, D. T. When thermoelectrics reached the nanoscale. *Nature Nanotechnology* **8,** 471–473. ISSN: 17483395 (2013).

23. Jiang, J.-W. & Park, H. S. Negative Poisson's Ratio in Single-Layer Black Phosphorus. *Nature Communications* **5,** 4727. ISSN: 2041-1723 (2014).

24. Xiang, Z. J. *et al.* Pressure-Induced Electronic Transition in Black Phosphorus. *Physical Review Letters* **115,** 1–5. ISSN: 10797114 (2015).

25. Isobe, H., Yang, B.-J., Chubukov, A., Schmalian, J. & Nagaosa, N. Emergent non-Fermi liquid at the quantum critical point of a topological phase transition in two dimensions. *Physical Review Letters* **116,** 076803. ISSN: 0031-9007 (2015).

26. Hu, J. *et al.* Band Gap Engineering in a 2D Material for Solar-to-Chemical Energy Conversion. *Nano Letters* **16,** 74–79. ISSN: 1530-6984 (2015).

27. Wang, H. *et al.* Ultrathin Black Phosphorus Nanosheets for Efficient Singlet Oxygen Generation. *Journal of the American Chemical Society* **137,** 11376–11382. ISSN: 0002-7863 (2015).

28. Abbas, A. N. *et al.* Black phosphorus gas sensors. *ACS nano* **9,** 5618–24. ISSN: 1936-086X (2015).

29. Köpf, M. *et al.* Access and in situ growth of phosphorene-precursor black phosphorus. *Journal of Crystal Growth* **405,** 6–10. ISSN: 00220248 (2014).

30. Jiang, Q. *et al.* Facile Synthesis of Black Phosphorus: an Efficient Electrocatalyst for the Oxygen Evolving Reaction. *Angewandte Chemie International Edition* **128,** 14053–14057. ISSN: 14337851 (2016).

31. Sun, L.-Q. *et al.* Electrochemical Activity of Black Phosphorus as an Anode Material for Lithium-Ion Batteries. *The Journal of Physical Chemistry C* **116,** 14772–14779. ISSN: 1932-7447 (2012).

32. Park, C.-M. & Sohn, H.-J. Black Phosphorus and its Composite for Lithium Rechargeable Batteries. *Advanced Materials* **19,** 2465–2468. ISSN: 09359648 (2007).

33. Castellanos-Gomez, A. *et al.* Isolation and characterization of few-layer black phosphorus. *2D Materials* **1,** 025001. ISSN: 2053-1583 (2014).

34. Hanlon, D. *et al.* Liquid exfoliation of solvent-stabilized few-layer black phosphorus for applications beyond electronics. *Nature Communications* **6.** ISSN: 20411723 (2015).

35. Ziletti, A *et al.* Phosphorene oxides: bandgap engineering of phosphorene by oxidation. *Physical Review B* **91,** 085407 (2015).

36. Ziletti, a, Carvalho, A, Campbell, D. K., Coker, D. F. & Castro, a. H. Oxygen defects in phosphorene. *Physical Review Letters* **114,** 046801. ISSN: 10797114 (2015).

37. Favron, A. *et al.* Photooxidation and quantum confinement effects in exfoliated black phosphorus. *Nature Materials* **14,** 1–8. ISSN: 1476-1122 (2015).

38. Wood, J. D. *et al.* Effective Passivation of Exfoliated Black Phosphorus Transistors Against Ambient Degradation. *Nano letters* **14,** 6964–6970 (2014).

39. Edmonds, M. T. *et al.* Creating a Stable Oxide at the Surface of Black Phosphorus. *ACS Applied Materials & Interfaces* **7,** 14557–14562. ISSN: 1944-8244 (2015).

40. Alsaffar, F. *et al.* Raman Sensitive Degradation and Etching Dynamics of Exfoliated Black Phosphorus. *Scientific Reports* **7,** 44540. ISSN: 2045-2322 (2017).

41. Zhang, C. D. *et al.* Surface Structures of Black Phosphorus Investigated with Scanning Tunneling Microscopy. *The Journal of Physical Chemistry C* **113,** 18823–18826. ISSN: 1932-7447 (2009).

42. Favron, A., Francoeur, S., Leonelli, R. & Martel, R. *Photostability of thin exfoliated black phosphorus* in *APS March Meeting 2014* (2014).

43. Li, Q. *et al.* On-surface synthesis: a promising strategy toward the encapsulation of air unstable ultra-thin 2D materials. *Nanoscale.* ISSN: 2040-3364 (2018).

44. Li, Q. *et al.* Covalent Functionalization of Black Phosphorus from First-Principles. *Journal of Physical Chemistry Letters* **7,** 4540–4546. ISSN: 19487185 (2016).

45. Yang, B. *et al.* Te-Doped Black Phosphorus Field-Effect Transistors. *Advanced Materials* **28,** 9408–9415. ISSN: 15214095 (2016).

46. Carvalho, A. & Neto, A. H. C. Phosphorene: Overcoming the Oxidation Barrier. *ACS Central Science* **1,** 289–291. ISSN: 2374-7943 (2015).

47. Yau, S.-l., Moffat, T. P., Bard, A. j., Zhang, Z. & Lerner, M. M. STM of the (010) surface of orthorombic phosphorus. *Chemical Physics Letters* **198,** 384–388 (1992).

48. Hu, Z. *et al.* Water-Catalyzed Oxidation of Few-Layer Black Phosphorous in a Dark Environment. *Angewandte Chemie - International Edition* **56,** 9131–9135. ISSN: 15213773 (2017).

49. Zhou, Q., Chen, Q., Tong, Y. & Wang, J. Light-Induced Ambient Degradation of Few-Layer Black Phosphorus: Mechanism and Protection. *Angewandte Chemie International Edition* **55,** 1–6. ISSN: 14337851 (2016).

50. Luo, W. *et al.* Surface chemistry of black phosphorus under a controlled oxidative environment. *Nanotechnology* **27,** 434002. ISSN: 1361-6528 (2016).

51. Huang, Y. *et al.* Interaction of black phosphorus with oxygen and water. *Chemistry of Materials* **28,** 8330–8339. ISSN: 15205002 (2016).

52. Walia, S. *et al.* Defining the role of humidity in the ambient degradation of few-layer black phosphorus. *2D Materials* **4,** 1–8. ISSN: 2053-1583 (2017).

53. Wang, Y. *et al.* Degradation of black phosphorus: a real-time 31 P NMR study. *2D Materials* **3,** 035025. ISSN: 2053-1583 (2016).

54. Chen, L. *et al.* Scalable Clean Exfoliation of High-Quality Few-Layer Black Phosphorus for a Flexible Lithium Ion Battery. *Advanced Materials* **28,** 510–517. ISSN: 15214095 (2016).

55. Watts, J. F. & Wolstenholme, J. *An Introduction to Surface Analysis by XPS and AES* 2nd. ISBN: 0470847131 (Wiley, May 2003).

56. Wandelt, K. Photoemission studies of adsorbed oxygen and oxide layers. *Surface Science Reports* **2,** 1–121 (Sept. 1982).

57. Crumlin, E. J., Bluhm, H. & Liu, Z. In situ investigation of electrochemical devices using ambient pressure photoelectron spectroscopy. *Journal of Electron Spectroscopy and Related Phenomena* **190,** 84–92. ISSN: 03682048 (2013).

58. Bluhm, H. Photoelectron spectroscopy of surfaces under humid conditions. *Journal of Electron Spectroscopy and Related Phenomena* **177,** 71–84. ISSN: 03682048 (2010).

59. Polack, F. *et al.* TEMPO: A new insertion device beamline at SOLEIL for time resolved photoelectron spectroscopy experiments on solids and interfaces. *AIP Conference Proceedings* **1234,** 185–188. ISSN: 0094243X (2010).

60. Giannozzi, P. *et al.* QUANTUM ESPRESSO: A modular and open-source software project for quantum simulations of materials. *Journal of Physics Condensed Matter* **21.** ISSN: 09538984 (2009).

61. Perdew, J. P., Burke, K. & Ernzerhof, M. Generalized Gradient Approximation Made Simple. *Physical Review Letters* **77,** 3865–3868. ISSN: 10797114 (1996).

62. Becke, A. D. & Johnson, E. R. Exchange-hole dipole moment and the dispersion interaction revisited. *Journal of Chemical Physics* **127,** 0–6. ISSN: 00219606 (2007).

63. Otero-De-La-Roza, A. & Johnson, E. R. Van der Waals interactions in solids using the exchange-hole dipole moment model. *Journal of Chemical Physics* **136.** ISSN: 00219606 (2012).

64. Marzari, N., Vanderbilt, D., De Vita, A. & Payne, M. C. Thermal contraction and disordering of the al(110) surface. *Physical Review Letters* **82,** 3296–3299. ISSN: 10797114 (1999).

65. Pehlke, E. & Scheffler, M. Evidence for site-sensitive screening of core holes at the Si and Ge (001) surface. *Physical Review Letters* **71,** 2338–2341. ISSN: 00319007 (1993).

66. Casalongue, H. S. *et al.* Direct observation of the oxygenated species during oxygen reduction on a platinum fuel cell cathode. *Nature Communications* **4,** 2817. ISSN: 2041-1723 (2013).

67. Tanuma, S., Powell, C. J. & Penn, D. R. Calculation of electron inelastic mean free paths (IMFPs) VII. Reliability of the TPP-2M IMFP predictive equation. *Surface and Interface Analysis* **35,** 268–275. ISSN: 01422421 (2003).

68. Cabrera, N & Mott, N. F. Theory of the oxidation of metals. *Reports on Progress in Physics* **12,** 163–184. ISSN: 00344885 (Jan. 1949).

69. Atkinson, A. Transport processes during the growth of oxide films at elevated temperature. *Reviews of Modern Physics* **57,** 437–470. ISSN: 00346861 (1985).

70. Gaskell, K. J., Smith, M. M. & Sherwood, P. M. A. Valence band x-ray photoelectron spectroscopic studies of phosphorus oxides and phosphates. *Journal of Vacuum Science & Technology A: Vacuum, Surfaces, and Films* **22,** 1331–1336. ISSN: 0734-2101 (2004).

71. Kim, K. K., Kim, H. S., Hwang, D. K., Lim, J. H. & Park, S. J. Realization of p-type ZnO thin films via phosphorus doping and thermal activation of the dopant. *Applied Physics Letters* **83,** 63–65. ISSN: 00036951 (2003).

72. Zhang, Z. & Yates, J. T. Band bending in semiconductors: chemical and physical consequences at surfaces and interfaces. *Chemical reviews* **112,** 5520–51. ISSN: 1520-6890 (Oct. 2012).

73. Yeh, J. J. & Lindau, I. Atomic subshell photoionization cross sections and asymmetry parameters: 1 Z 103. *Atomic Data and Nuclear Data Tables* **32,** 1–155. ISSN: 10902090 (1985).

Appendix A

Spectrum quantification

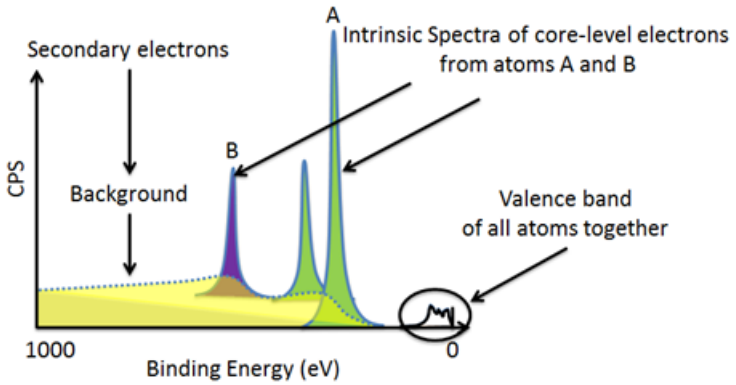

Figure A.1: Typical XPS spectrum. Where we have intrinsic peaks attributed to orbitals of atoms A and B. Where the A atom's orbital is subject to spin-orbit coupling, hence the double peaks. It is present also the background (secondary electrons) and the valence band total of all atoms probed.

A XPS experiment yields results in the form of a spectrum of counts per second per binding energy. It presents peaks and features related to electrons of the probed atoms. Figure A.1 shows an example of a typical XPS spectrum. There are three main features on a XPS spectrum, the intrinsic peaks, the valence band and the background.

As explained in the Chapter 2.2, when a surface is illuminated by an X-ray, electrons can be photo-emitted. Their kinetic energies are intrinsically related to their orbital and atom's atomic number. The intrinsic peaks in Figure A.1 are related to the electrons coming from the core-levels of an atom, these peaks represent uniquely one orbital of a particular atom. Since valence band levels of many different atoms have very similar binding energies close to the Fermi-level, the valence band will not represent peaks of a single atom, and rather represent the convolution of many valence band orbitals from all the atoms probed.

Some of the photo-emitted electrons suffer inelastic events along the way towards the analyzer, losing part of its kinetic energy. These electrons with lower kinetic energy are designated secondary electrons, responsible for the spectrum's background. In order to remove the influence of this phenomenon, a background filter must be applied to the spectrum's region

of interest. A filter with the *Shirley* algorithm is the most widely used and most adequate, and thus was used during the analysis of this project.

The main characteristics of a XPS peak are its full width height medium (FWHM), its position (binding energy) and its area (number of counts). These features are shown in Figure A.2.

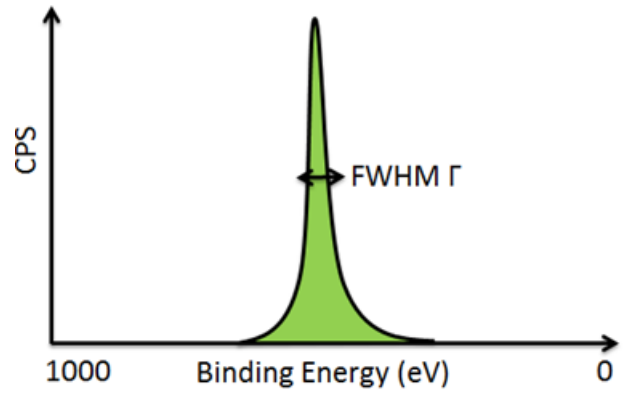

Figure A.2: Typical XPS peak, with its full width height medium (FWHM) or Γ, its area (green region) and its binding energy position.

It is necessary to choose a curve for the fitting of the peaks present in the spectrum. The photoemission process of an electron encompasses several steps that determine the shape of its spectral line. After the photoemission, the hole left by the electron in the atom's electronic cloud has a finite lifetime. The finitude of the lifetime promotes an intrinsic uncertainty in the determination of the electron's kinetic energy, due to the Heisenberg's uncertainty principle. This uncertainty broadens the peak in the form of a Lorentzian curve.

Uncertainties related to the experiment by itself, such as the energy resolution, vibrational modes and statistics, contribute to the broadening of the XPS peak with a Gaussian curve shape.

Therefore, to better suit the peak, the fitting must be performed with a curve that is a convolution of a Gaussian curve with a Lorentzian curve. The weights of each curve are experimentally determined for a specific experiment.

The area under the adjusted curve is denominated the peak's intensity, collecting the signal from all photo-emitted electrons. This intensity in its turn is proportional to some factors as it is shown in Equation A.1.

$$I_0 \approx F(h\nu) * N * \sigma(h\nu) * T(KE) \tag{A.1}$$

The peak's intensity in its turn is proportional to the photon flux of the source in a determined energy ($F(h\nu)$), to the number of atoms being probed (N), to the photoemission effective cross section of the atom's orbital (σ) and the total transmission of the analyser for an electron with determined kinetic energy ($T(KE)$).

Appendix B

Stoichiometry calculations

In Appendix A we discussed how the intensity of a XPS peak depends primarily of 4 factors: $I_0 \approx F(h\nu) * N * \sigma(h\nu) * T(KE)$, photon source flux ($F(h\nu)$), number of atoms ($N$), effective photoemission cross-section (σ) and total transmission of the analyser for electron's kinetic energy ($T(KE)$). Since the peak's intensity is directly proportional to the number of atoms being probed, one can obtain relative quantities between the different atoms of the mix. Imagine a case where we are probing a phosphorus oxide, containing both oxygen (O) and phosphorus atoms in a stoichiometry of N_O/N_P.

Therefore, after a supposed XPS measurement, we have a spectra with peaks related to the oxygen 1s orbital (O) and to the phosphorus 2p orbital (P). Their intensities are given by Equations B.1 and B.2 respectively.

$$I_O \approx F(h\nu_O) * N_O * \sigma_O(h\nu_O) * T(KE_O) \tag{B.1}$$

$$I_P \approx F(h\nu_P) * N_P * \sigma_P(h\nu_P) * T(KE_P) \tag{B.2}$$

Dividing one intensity by the other we obtain Equation B.3, referring to the atoms' numbers ratio N_O/N_P.

$$\frac{N_O}{N_P} = \frac{I_O}{I_P}\left(\frac{F(h\nu_P)\sigma_P(h\nu_P)T(KE_P)}{F(h\nu_O)\sigma_O(h\nu_O)T(KE_O)}\right) \tag{B.3}$$

The following approach for solving the stoichiometry takes into account the use of a synchrotron source. Nevertheless, it is also possible to do it in a conventional XPS setup, despite requiring a more advanced method for acquiring the total transmission of the analyzer for different electron kinetic energies.

The intensities (I_P and I_O) are obtained experimentally by calculating the area underneath the fitted peak of the XPS spectra. Furthermore, the photon flux of the source is almost always tabulated by the line scientists for the entire energy of the synchrotron line. If not, a simple flux measurement for the desired energy can be performed. In our case, the photon flux of

the TEMPO beamline of the synchrotron SOLEIL is already tabulated. The effective photoionization cross-section of both the phosphorus 2p and oxygens 1s orbitals have already been calculated several times in the literature for various incoming photon energies. We used the data from Yeh [73]. In particular, we had to use the anisotropy corrected values, since we were on orthogonal incidence instead of the magic angle.

The 1s orbital of oxygen has binding energies of around 530 eV. Meanwhile, the 2p orbital of phosphorus presents binding energies around 130 eV. We measured O_{1s} with an incident photon energy of 730 eV and P_{2p} with 330 eV. Therefore, we have both atoms photoemitting electrons with kinetic energies of around 200 eV. Furthermore, it is possible to eliminate the dependency of Equation B.3 of $T(KE_O)$ and $T(KE_P)$, since both these transmission are respective to the same electron's kinetic energy (200 eV), and thus cancel each other out. Equation B.3 is then reduced to B.4.

$$\frac{N_O}{N_P} = \frac{I_O}{I_P}\left(\frac{F(330eV)\sigma_P(330eV)}{F(330eV)\sigma_O(730eV)}\right) \tag{B.4}$$

Using the values for photon flux and anisotropy corrected cross-section for these energies, Equation B.4 turns into B.5.

$$\frac{N_O}{N_P} = \frac{I_O}{I_P} * 0.95 \pm 0.06 \tag{B.5}$$

Therefore, the stoichiometry is this situation will be given by the ratio between the intensities of the oxygen and phosphorus peaks multiplied by a factor of 0.95.

Appendix C

Kinetic equations derivations

In our black phosphorus oxidation model, the following reactions occur:

$$\mathrm{BP} + \mathrm{O_2} \xrightarrow{\mathrm{k_1, h\nu}} \mathrm{BP} + \mathrm{O^*}$$

$$\mathrm{O^*} + \mathrm{BP} \xrightarrow{\mathrm{k_2^P}} \mathrm{PO}$$

Of these reactions, using the parallel reactions model, we obtain the differential equations for the black phosphorus (BP), oxygen gas (O_2), phosphorene oxide (PO) and reactive oxygen species (O_2^*). As a function of the reaction rates k_1 and k_2:

$$\frac{d[O_2]}{dt} = -k_1[O_2][BP] \tag{C.1}$$

$$\frac{BP}{dt} = -k_2[BP][O_2^*] \tag{C.2}$$

$$\frac{d[O_2^*]}{dt} = k_1[BP][O_2] - k_2[O_2^*][BP] \tag{C.3}$$

$$\frac{d[PO]}{dt} = k_2[O_2^*][BP] \tag{C.4}$$

We have that the concentration of $[O_2]$ won't alter, since the chamber's atmosphere control represents an infinite supply of molecules. Therefore, it's differential is 0. Resolving the remaining differential equations for the phosphorene oxide (PO) concentration we have that:

$$[PO](t) = [BP]_0 \left(1 + \frac{k_1 e^{-k_2(t)} - k_2 e^{-k_1 t}}{k_2 - k_1}\right) \tag{C.5}$$

However, the rate of consumption (k_2) of the reactive oxygen species (O_2^*) is much greater than the rate of photo-activation (k_1), since the process of photo-activation by X-ray is an inefficient process, and reactive oxygen species are known to readily react. We then assume

that $k_1 << k_2$, reducing the equation to:

$$[PO](t) = [BP]_0(1 - e^{-k_1 t} \tag{C.6}$$

The black phosphorus layers involved in this reaction will be consumed to form the phosphorene oxide. Therefore, we can say that $[PO]/[BP]_0 = \theta$, where θ is rate of oxide coverage.

$$\theta(t) = (1 - e^{-k_1 t}) \tag{C.7}$$

That is the equation representing the kinetics of oxide growth for our experimental conditions. The same line thought can be applied to the carbon reduction oxidation reaction:

$$\mathrm{BP} + \mathrm{O_2} \xrightarrow{\mathrm{k_1},\, \mathrm{h}\nu} \mathrm{BP} + \mathrm{O^*}$$

$$\mathrm{O^*} + \mathrm{C} \xrightarrow{\mathrm{k_2^C}} \mathrm{CO_{2(gas)}}$$

Which differential equations are:

$$\frac{d[O_2]}{dt} = -k_1[O_2][BP] \tag{C.8}$$

$$\frac{BP}{dt} = -k_{2C}[BP][O_2^*] \tag{C.9}$$

$$\frac{d[O_2^*]}{dt} = k_1[BP][O_2] - k_{2C}[O_2^*][C] \tag{C.10}$$

$$\frac{d[CO_2]}{dt} = k_{2C}[O_2^*][C] \tag{C.11}$$

Solving for $[C]$ we have that:

$$[C](t) = \left(\frac{k_1 e^{-k_{2C}(t)} - k_{2C} e^{-k_1 t}}{k_{2C} - k_1}\right) \tag{C.12}$$

Using $k_1 << k_2$ we then get to:

$$C(t) = e^{-k_1 t} \tag{C.13}$$

That is the carbon reduction equation.

Appendix D

Depth profile modeling

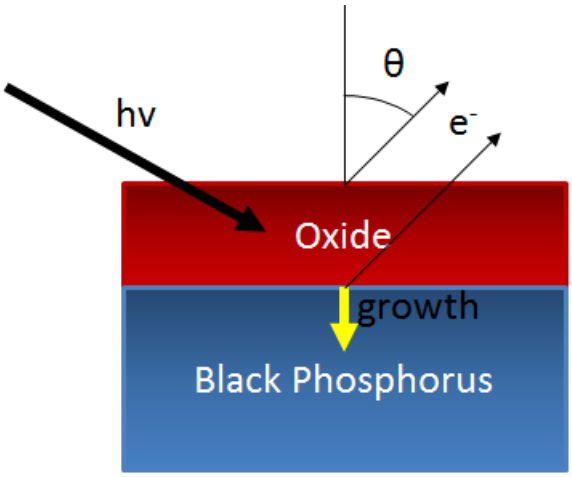

Figure D.1: Model of the depth profile of a complete oxide layer at the surface of black phosphorus growing in thickness. With the incident photon ($h\nu$), outgoing electrons (e^-) and oxide thickness (τ).

We can model the heterogeneous model with an oxide layer of thickness τ growing across the surface of black phosphorus flake (Figure D.1). Electrons coming from the black phosphorus underneath will be attenuated by the surface layers. Since the black phosphorus and phosphorene oxide will attenuate the electrons at almost the same rate, we approximate the inelastic mean free path of the electrons on both these structures as the same λ. Hence, the intensity of these electrons will be for black phosphorus (according to chapter 3.1):

$$I_{BP} = I_{BP,0} * e^{-\frac{\tau}{\lambda \cos\theta}} \tag{D.1}$$

Where θ is the angle between the electrons trajectory and the surface's normal. While that for the oxide we have that:

$$I_{Ox} = I_{Ox,0} \left(1 - e^{-\frac{\tau}{\lambda \cos\theta}}\right) \tag{D.2}$$

If we divide equation D.2 by equation D.1, we have that:

$$\frac{I_{Ox}}{I_{BP}} = \frac{I_{Ox,0}}{I_{BP,0}} \left(e^{\frac{\tau}{\lambda \cos\theta}} - 1 \right) \tag{D.3}$$

If we substitute $\frac{I_{Ox,0}}{I_{BP,0}}$ for α, since it is a constant, equation D.3 furthers simplifies to:

$$\frac{I_{Ox}}{I_{BP}} = \alpha \left(e^{\frac{\tau}{\lambda \cos\theta}} - 1 \right) \tag{D.4}$$

That is the equation we used to fit the data of the depth profile in order to obtain the thickness of the oxide.